

MHD Simulation of a Disk Subjected to Lense-Thirring Precession

Kareem A. Sorathia¹, Julian H. Krolik¹

and

John F. Hawley²

ABSTRACT

When matter orbits around a central mass obliquely with respect to the mass's spin axis, the Lense-Thirring effect causes it to precess at a rate declining sharply with radius. Ever since the work of Bardeen & Petterson (1975), it has been expected that when a fluid fills an orbiting disk, the orbital angular momentum at small radii should then align with the mass's spin. Nearly all previous work has studied this alignment under the assumption that a phenomenological "viscosity" isotropically degrades fluid shears in accretion disks, even though it is now understood that internal stress in flat disks is due to anisotropic MHD turbulence. In this paper we report a pair of matched simulations, one in MHD and one in pure (non-viscous) HD in order to clarify the specific mechanisms of alignment. As in the previous work, we find that disk warps induce radial flows that mix angular momentum of different orientation; however, we also show that the speeds of these flows are generically transonic and are only very weakly influenced by internal stresses other than pressure. In particular, MHD turbulence does not act in a manner consistent with an isotropic viscosity. When MHD effects are present, the disk aligns, first at small radii and then at large; alignment is only partial in the HD case. We identify the specific angular momentum transport mechanisms causing alignment and show how MHD effects permit them to operate more efficiently. Lastly, we relate the speed at which an alignment front propagates outward (in the MHD case) to the rate at which Lense-Thirring torques deliver angular momentum at smaller radii.

Subject headings: accretion disks, turbulence

¹Department of Physics and Astronomy, Johns Hopkins University, Baltimore, MD 21218, USA

²Department of Astronomy, University of Virginia, Charlottesville VA 22904, USA

1. Introduction

There are many reasons why accretion disks around rotating masses may not be aligned with the spin axis of the central mass. If the matter is supplied from a companion star, the orbital plane of the binary may be oblique; if the matter is supplied from the interstellar medium, its mean orbital plane may similarly be inclined; if the matter is supplied from a tidally-disrupted star, the orbital plane should be entirely uncorrelated with the black hole spin. Whatever the origin of the misalignment, general relativity predicts that there is a torque exerted on the orbiting material. To lowest post-Newtonian order, the torque on an orbiting ring of radius r and angular momentum \mathbf{L} is $2(G/c^2)\mathbf{J} \times \mathbf{L}/r^3$ when the spin angular momentum of the central mass is \mathbf{J} ; the result is precession about the central mass’s spin axis at a rate $\omega = 2G|\mathbf{J}|/(r^3c^2)$. The precession rate is most interesting, of course, when r is not an extremely large number of gravitational radii $r_g \equiv GM/c^2$, so the effect is normally associated with black holes, or perhaps neutron stars.

Because the torque grows so rapidly with smaller r , it has been supposed ever since the truly seminal paper of Bardeen & Petterson (1975) that the strong differential precession at small radii will induce internal disk friction, causing the inner part of the disk to settle into the equatorial plane of the central mass’s rotation. Papaloizou & Pringle (1983) invented an angular momentum-conserving formalism to encompass this picture, in which they pointed out that local disk warps can be smoothed hydrodynamically because the warps create radial pressure gradients by shifting neighboring rings vertically relative to one another. Radial fluid motions are then induced, which can mix the differently-oriented angular momenta of the adjacent rings. The question that arises, however, is how to relate the radial velocities to the radial pressure gradients. Papaloizou & Pringle (1983) proposed that when the disk is very thin, the flow velocities would be limited by the same “viscosity” accounting for angular momentum transport in flat disks, but operating isotropically on all shears. Conversely, they argued, when the disk is relatively thick, this “viscosity” would damp bending waves. Pringle (1992) constructed a simpler vehicle for analyzing this geometrically complicated problem, heuristically separating the angular momentum transport into two pieces. The first of these was the radial transport of angular momentum due directly to the action of the isotropic viscosity. The second was a lumped-parameter description of the evolution of local warps, in which they were supposed to be smoothed diffusively. Following Papaloizou & Pringle (1983), Pringle (1992) argued that the diffusivity for local warps would scale inversely with the putative isotropic viscosity. Ogilvie (1999) developed a nonlinear theory linking the mutual scaling of the two transport coefficients. When the viscosity is normalized to the local pressure via the dimensionless coefficient α , Ogilvie (1999) confirmed the expected inverse scaling for small values of α , but found a somewhat more complicated relation for larger values, provided $\alpha < 1$. It is therefore natural to describe the magnitude of the diffusion co-

efficient in the same pressure-normalized fashion, scaling it in terms of α_2 (Lodato & Pringle 2007). Nelson & Papaloizou (2000) performed SPH simulations in which the numerical diffusion of the algorithm provided an effective isotropic viscosity and found behavior more or less in keeping with these expectations, but Lodato & Pringle (2007) and Lodato & Price (2010), using an explicit isotropic viscosity, argued that α_2 was limited to be $\lesssim 3$, and also found that a diffusive description did not well match the evolution of their simulations when the warp was “nonlinear” (see § 3.2 for the definition of “nonlinear” in this context). Perhaps more surprisingly, the recent SPH simulations of Nixon et al. (2012) develop sharp breaks in the disk profile when the degree of misalignment is large.

There is, however, a fundamental worry concerning this entire approach: the assumption that an isotropic viscosity acts in accretion disks. For more than fifteen years (Balbus & Hawley 1991; Hawley et al. 1995; Brandenburg et al. 1995; Stone et al. 1996; Balbus & Hawley 1998), it has been clear that the angular momentum transport governing accretion is *not* due to any sort of viscosity, but rather to MHD turbulence driven by the magneto-rotational instability. These stresses, although related in the mean to orbital shear, are far from isotropic (Stone et al. 1996; Hawley et al. 2011), do not scale linearly with the shear, and do not respond in any direct way to fluctuating shears (Pessah et al. 2008). In fact, when radial motions are sheared vertically in a magnetized orbiting plasma, they are unstable when, as is the case here, the vertical scale of the shear is longer than the distance an Alfvén wave travels in a dynamical time (Balbus & Hawley 1991). All these contrasts call into question whether, or under what circumstances, MHD-derived stresses might either limit radial flows or damp bending waves. To date, only one numerical simulation has been used to investigate the effects produced by Lense-Thirring torques on disks with internal MHD turbulence (Fragile et al. 2007), but its interpretability was limited by the nearness of the disk to the innermost stable circular orbit, the disk’s relatively large scale height, and the difficulty of adequately resolving the MHD turbulence. Thus, the applicability of this central assumption to the theory is still unclear.

In addition to this concern, there is also another reason to revisit the dynamics of the Bardeen-Petterson problem. Despite all the effort devoted to its study, there is still no clear understanding of angular momentum flows during the process of inner-disk alignment. If the angular momentum given the disk material by the Lense-Thirring torque remained with the material initially receiving it, the matter would simply precess around the central mass’s spin axis while very gradually drifting inward (this was, in fact, the way Bardeen & Petterson (1975) originally envisioned it). On the other hand, if hydrodynamic effects redistribute the angular momentum given the disk by the torques (Papaloizou & Pringle 1983), where does it go? Could the MHD turbulence carry the unaligned angular momentum a substantial distance? Moreover, why should that redistribution lead to alignment? After all, averaged

over many precession periods, the net integrated angular momentum due to the torque goes to zero.

To begin answering these questions, we have performed a new MHD simulation of a disk evolving under the influence of Lense-Thirring torques. In its definition, we have made the strategic decision to forego a fully relativistic treatment so that the computational effort can be focused on resolving the MHD turbulence in a reasonably thin disk and running for a sufficiently long time, rather than on the dynamical complications of general relativity. It therefore assumes Newtonian dynamics except for a single term expressing the gravitomagnetic torque to lowest post-Newtonian order. We have also chosen parameters such that the precession rate in the middle of the disk is slower than the orbital period, but rapid enough that the mid-point of the disk (if unencumbered by hydrodynamics) would precess through a full rotation over the course of the simulation. The Newtonian approximation is an advantage here, too, because such a comparatively rapid precession rate is found in a genuine relativistic context only in the region not far outside the ISCO, where the warp dynamics would be obscured by a mass inflow rate comparable to the precession frequency.

2. Simulations

The simulation code we employ is a contemporary translation (in Fortran-95) of the 3D finite-difference MHD code *Zeus* (Stone & Norman 1992a,b). The magnetic field is updated using the “method of characteristics constrained transport (MOCCT)” algorithm to maintain zero divergence to machine accuracy (Hawley & Stone 1995). The *Zeus* code solves the standard equations of Newtonian fluid dynamics, but we augment its momentum equation with a term of the form $\rho \mathbf{v} \times \mathbf{h}$ to represent the gravitomagnetic force per unit mass, where ρ is the mass density, \mathbf{v} is the fluid velocity, and

$$\mathbf{h} = \frac{2\mathbf{J}}{r^3} - \frac{6(\mathbf{J} \cdot \mathbf{r})\mathbf{r}}{r^5}. \quad (1)$$

Here \mathbf{J} represents the magnitude and direction of the spin vector of the central mass and r is spherical radius.

In this paper we report two simulations, one employing full 3D MHD, but the other purely hydrodynamic so that we may identify the special properties due to MHD through contrasting the two. The initial condition for the MHD simulation is a hydrostatic torus orbiting a point-mass in Newtonian gravity (see Hawley (2000)) defined by the parameters $q = 1.65$, $r_{in} = 7.5$, $r_M = 10$, $\rho_M = 100$, and $\Gamma = 5/3$. That is, in this initial state the orbital frequency $\Omega \propto R^{-q}$ for cylindrical radius R , and the disk extends from an inner radius r_{in} to an outer radius $r_{out} \simeq 14$. Its pressure maximum is found at r_M , where the density is ρ_M . We

assume an adiabatic equation of state with index Γ . This combination of parameters results in a disk whose aspect ratio $H/R \simeq 0.06$ – 0.1 over its entire radial extent when H is defined as $\sqrt{2}c_{s0}/\Omega$, for c_{s0} the isothermal sound speed. Equivalently, the angle subtended by one scale-height is $\simeq 4^\circ$ – 6° . The initial magnetic field in the disk is a set of nested poloidal field loops defined by the vector potential

$$A_\phi = \rho - \rho_C, \quad (2)$$

where $\rho_C = 0.1$ and $\mathbf{B} = \nabla \times \vec{A}$. The field is scaled so that the volume-integrated ratio of the gas to magnetic pressure, is initially 25.

At the beginning of the MHD simulation (which we call BP-m), we perturb the pressure with random fluctuations whose rms amplitude is $\simeq 1\%$. From these perturbations, the magneto-rotational instability grows, and we follow its development *without any external torques* for 15 orbits at r_M . At this point, the MHD turbulence is fully saturated. In addition, the internal stresses due to the anisotropy of the turbulence have led to significant disk spreading. Roughly a third of the initial disk mass is lost, mostly via accretion through the inner boundary of the simulation (at $r = 4$). In addition, dissipation associated with the artificial bulk viscosity necessary to describe shocks properly has heated the gas so that $H/R \simeq 0.12$ – 0.2 across most of its extent.

The Lense-Thirring torque is turned on only at this point, when the MHD turbulence has saturated. For reasons we explain momentarily, we choose the spin-axis of the central mass to lie two initial scale-heights (12°) away from the initial orbital axis. We set the magnitude of this torque so that $\omega(r_M)/\Omega(r_M) = 1/15$ for precession frequency ω and orbital frequency Ω . In terms of the exigencies of simulation, this is a very natural choice: $\omega \ll \Omega$ through all the disk except its innermost rings, but ω is not so small that to follow a precession period would take a prohibitively large amount of computer time. Regrettably, in terms of actual physics this is a very unnatural (and nominally inconsistent) choice because such a ratio is achieved in real life only when $r/r_g = \{6.1(a/M) \sin \theta [1 + \sqrt{1 + 0.133/\sin \theta}]\}^{2/3}$, where θ is the inclination angle between the orbital angular momentum and the central mass's spin angular momentum. Newtonian dynamics are, of course, a very poor approximation in such a location. We justify it, however, on the grounds that what is most important to our effort to elucidate disk response to Lense-Thirring torque is the ability to explore the consequences of significant precession while assuring that it is still significantly slower than the orbital frequency. For similar reasons, we also ignore the relativistic contribution to the apsidal precession rate, even though one contribution to it is independent of black hole spin and larger than the Lense-Thirring rate, while another contribution is comparable to the Lense-Thirring precession frequency. There are also two more reasons to ignore the relativistic apsidal precession. It is not the only mechanism causing the radial epicyclic frequency to

differ from the orbital frequency; radial pressure gradients also do this, and are likely to be at least as large, especially at the large distance from the black hole at which the Bardeen-Petterson transition radius is most likely to fall in real disks. In addition, because only part of the apsidal precession is proportional to black hole spin, our Newtonian approximation makes it impossible to scale the apsidal precession frequency with the Lense-Thirring (nodal) precession frequency.

We then follow the evolution of the disk for 15 orbits at r_M , i.e., one full precession period at r_M , or $T = 30\pi/\Omega_M$ (throughout the remainder of this paper, we will describe time in units of a “fiducial orbit”, the orbital period at r_M). Over the course of this torqued phase of evolution, $\simeq 10\%$ of the disk mass is accreted through the inner radial boundary. In addition, the heating associated with a large number of weak shocks increases its scale height by $\simeq 10\%$.

The contrasting hydrodynamic simulation (called **BP-h**) begins from an initial condition whose radial profiles of midplane density and midplane scale-height match the azimuthally-averaged values in the MHD simulation immediately before the torque is turned on. The vertical density structure is what would be expected in hydrostatic equilibrium:

$$\rho(R, z) = \rho_0(R) \exp \left[\frac{-z^2}{H^2(R)} \right], \quad (3)$$

where R is cylindrical radius and z is vertical distance away from the disk plane. The local pressure is simply $H^2(R)\Omega^2(R)\rho/2$. The velocity field is chosen so that it is Keplerian in the disk midplane, but the disk rotates on cylinders. Although the disk so defined is in vertical equilibrium, there are unbalanced radial pressure gradients, but they are relatively small.

For the hydrodynamic simulation, the torque begins immediately. Like the MHD simulation, it is run for 15 orbits at r_M .

Simulating a warped accretion disk using a grid-based method presents certain challenges. In a warped disk it is guaranteed that at least some orbital velocities are oblique to the grid coordinates, and this obliquity of the strongly supersonic flow must cause at least some numerical dissipation (see Sorathia et al. (2013) for numerical experiments quantifying these effects). We have made several choices designed to minimize this dissipation. Following the results of the numerical experiments in Sorathia et al. (2013), we adopt a spherical grid. We also align the initial orbital plane of **BP-m** with the equatorial plane of the coordinates in order to minimize numerical dissipation during the 15 orbits in which the MHD turbulence grows. This is also why we chose a relatively small inclination between the spin-axis and the initial orbital axis, and, as we are about to discuss, used as fine a resolution as possible.

The spatial domain for both simulations was $(r, \theta, \phi) \in [4, 28] \times \pi[0.2, 0.8] \times 2\pi[0, 1]$.

Recent work on convergence in MHD disk simulations (Hawley et al. 2011; Sorathia et al. 2012) has shown that at least 32 ZPH (Zones Per vertical scale Height) are required to approach convergence in flat disks. It is possible that the additional complexity of external torques and disk warping raise that standard, but no systematic studies yet exist to determine whether they do and to what degree. On the other hand, a sufficiently long simulation even with this minimal resolution requires a large amount of computer time. We have therefore chosen to just meet that standard (and our MHD simulation still consumed 1.3×10^6 processor-hours). Our spherical grid had (288, 384, 1024) cells in the radial, polar, and azimuthal directions respectively. In order to maximize our effective resolution in the regions we most care about, we space the cells logarithmically in the radial direction (i.e., $\Delta r/r$ is constant), uniformly in the azimuthal direction, and employ a polynomial spacing in the polar dimension (Eqn. 6 of Noble et al. (2010), with $\xi = 0.65$ and $n = 13$). This sort of polynomial spacing focuses cells near the equatorial plane, giving a resolution of more than 32 ZPH within $\pm 20^\circ$ of the midplane. At the pressure maximum of the torus, $r_M = 10$, the cell dimensions in the radial and polar directions are approximately equal, while the azimuthal cell dimensions are about a factor of 2 larger. We present detailed resolution quality data for this simulation in the Appendix.

The requirements for hydrodynamic resolution are not nearly so demanding because a purely hydrodynamic simulation is not turbulent. Although the flow is complicated, it is laminar, and has rather little structure on small spatial scales. Consequently, BP-h is well-resolved when run on a very similar grid to BP-m, but one whose cell dimensions are exactly twice as large in each dimension.

Boundary conditions for the two simulations are also identical. For hydrodynamic quantities, we use zero-gradient extrapolations and enforce an outwardly-directed velocity in the ghost zones. For the magnetic field, we set the transverse field components in the ghost zones to zero and require the normal component to satisfy the divergence-free constraint.

3. Results

At a qualitative level, the MHD and purely hydrodynamic simulations appear to resemble one another strongly. As we will emphasize throughout the remainder of this paper, the dominant mechanisms underlying the Bardeen-Petterson effect are *hydrodynamic*, not magneto-hydrodynamic. That being said, MHD does create an important difference between them whose consequences have numerous implications: the MHD system is turbulent, whereas the HD system is laminar.

3.1. Precession

The ultimate driver of the entire process is Lense-Thirring torque. To describe it, as well as the rest of the angular momentum flow, we use a Cartesian coordinate system (x, y, z) oriented to the central mass’s spin axis. That is, the z -direction is defined by the spin axis. The x direction in this system is defined so that the initial disk angular momentum is in the x - z plane with $L_x < 0$ and $L_z > 0$. In terms of these coordinates, the torque \mathbf{G} has only two non-zero components, G_x and G_y . Their dependence on radius and time is shown in Figures 1 (the x component) and 2 (the y component).

Both runs begin with $G_y < 0$ and relatively strong within $r \simeq 10$. Likewise in both cases G_y passes through zero and changes sign 5–6 orbits after the torque begins, becoming positive at later times. The only contrast in this regard is that G_y at late times is rather smaller in the MHD case. Similarly, a short time after the torque begins, G_x becomes positive in both cases, particularly for $r \lesssim 10$, but diminishes in magnitude with increasing time. A few orbits before the end of both simulations, G_x also changes sign, a couple of orbits earlier in BP-m than BP-h. In both cases, too, the time-integral of G_x is dominated by $r \lesssim 10$.

These trends reflect the progress of disk precession and alignment. We measure the precession angle at radius r by $\arctan[(\partial L_y/\partial r)/(\partial L_x/\partial r)]$, where the angular momentum partial derivatives are the angular momentum integrated on spherical shells at radius r . We measure the (mis)alignment angle β by $\arctan[(\partial L_\perp/\partial r)/(\partial L_z/\partial r)]$, where $L_\perp^2 = L_x^2 + L_y^2$. The sign change in G_y is associated with precession through an angle of $\pi/2$, while the decrease in magnitude in the torque is a signature of disk alignment. Figure 3 shows the precession in greater detail. Like the torque, of course, the precession rate in the two simulations is overall similar. However, they are by no means identical. When MHD effects operate, the mean disk precession is slightly faster than when they are absent. The largest precession angle at any radius found in BP-m after 15 orbits is $\simeq 1.4\pi$, but only $\simeq 1.1\pi$ in BP-h. Especially in the HD case, the precession is not far from solid-body, a result previously seen in other simulations (Nelson & Papaloizou 2000; Fragile & Anninos 2005; Fragile & Blaes 2008). After 2–3 orbits of torque, the color contours for BP-h run almost flat across the radius–time plane. Differential precession is weak in an absolute sense in BP-m, but nonetheless noticeably stronger than in BP-h. For the first $\simeq 5$ orbits, compared to BP-h it precesses more rapidly at small radii, but more slowly at large. These contrasts diminish over time. At the end of the simulation, the contrast in precession angle across the entire radial span even in BP-m is only $\simeq 0.4\pi$, even though the precession phase difference between test-particles at $r = 10$ and $r = 20$ would have been $15\pi/8$, and between $r = 5$ and $r = 10$, 15π ! The rate of this approximate solid-body precession corresponds to the test-particle precession frequency at $r \simeq 11.5$, slightly outside the pressure maximum, and rather close

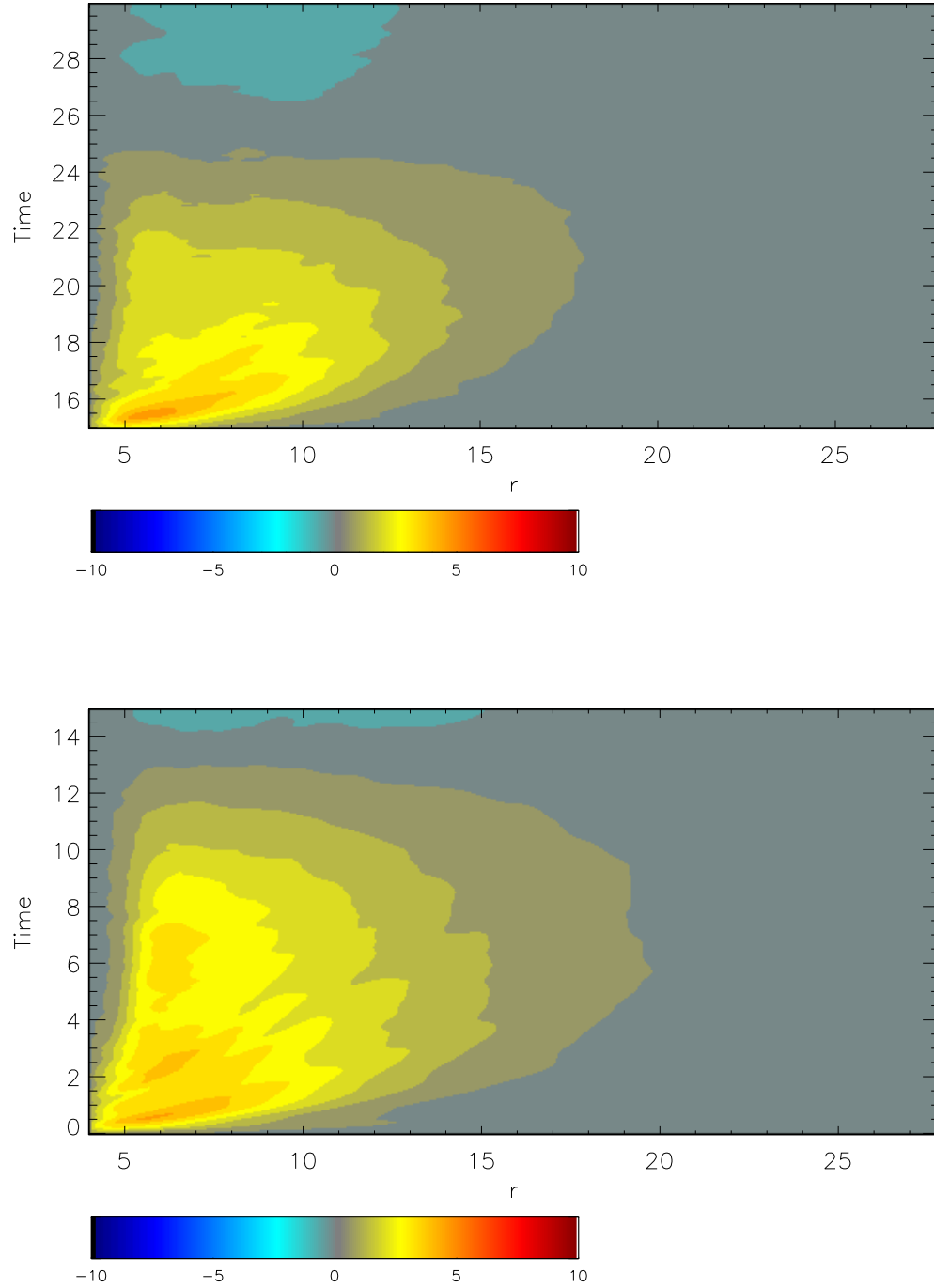


Fig. 1.— Color contours (see color bar) of G_x as a function of radius and time. Upper panel is BP-m; lower panel is BP-h.

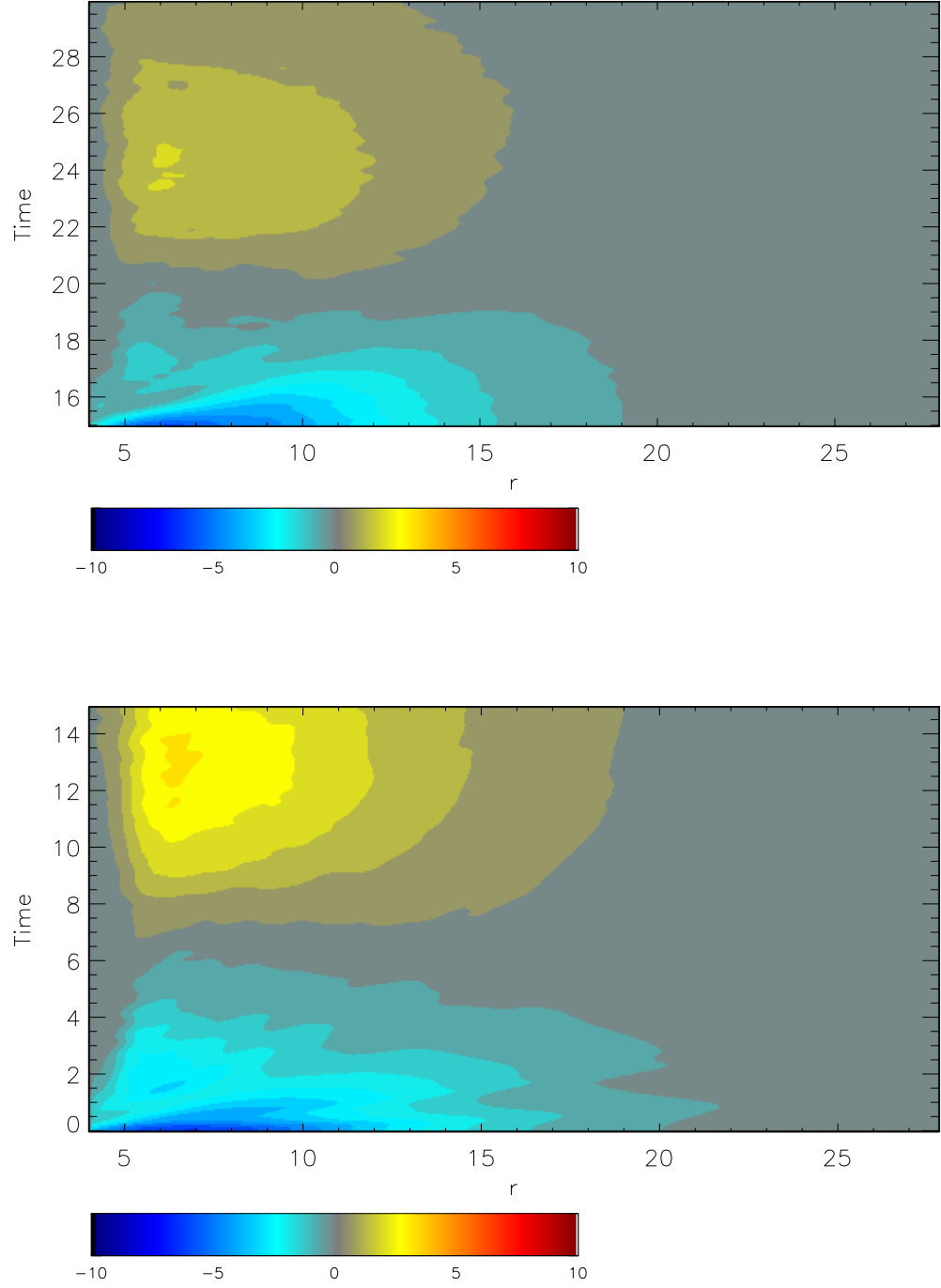


Fig. 2.— Color contours (see color bar) of G_y as a function of radius and time. Upper panel is BP-m; lower panel is BP-h.

to the radius corresponding to the mean specific angular momentum of the disk.

On the other hand, although the end-result is nearly solid-body precession, there are noticeable departures from rigid precession, particularly in BP-m (a possible explanation for why the MHD case is farther from solid-body precession than the HD case will be presented in § 3.2). As expected, the sense of the contrast is almost monotonic—outer rings precess more slowly than inner rings. This sense is not without exception, however—in the inner disk there can be small departures from monotonicity at the $\simeq 0.1\pi$ level.

Over much of the region where the disk departs from solid-body precession, the slope of the contours of fixed precession angle is very nearly constant at $\simeq 1.5$ length units per fiducial orbital period. Because the disk is close to precessing at a single rate, this near-constant slope translates to a near-constant twist rate: $\partial\phi/\partial r \simeq 0.14$ radians per radial length unit.

3.2. Local warping

The degree of local warp can be quantified in terms of

$$\hat{\psi} \equiv \frac{|d\mathbf{l}/d\ln r|}{H/r}, \quad (4)$$

where $\mathbf{l}(r) \equiv \mathbf{L}(r)/|\mathbf{L}(r)|$ is the direction of the angular momentum \mathbf{L} at radius r . When we compute $\hat{\psi}$, we use the actual value of H at that location and time. As shown initially in Nelson & Papaloizou (2000) and discussed at greater length in Sorathia et al. (2013), the magnitude of this quantity relative to unity gives a good indication of the degree of nonlinearity of the warp. That is, the radial contrast in pressure across a distance $\sim r$ becomes order unity when $\hat{\psi} \sim 1$ so that the speed of the corresponding radial flow becomes transonic.

Sorathia et al. (2013) found a further significance for $\hat{\psi} \gtrsim 1$: the rate at which warps decay as a result of the angular momentum mixing associated with these radial flows increases sharply when $\hat{\psi}$ becomes greater than unity. That finding also applies to these simulations. Despite the strong radial-dependence of the precession frequency, $d\mathbf{l}/d\ln r$ never exceeds $\simeq 0.6$ in either simulation; test-particle precession would have made this figure $\simeq 50$ between $r = 5$ and $r = 10$ by the end of the simulation.

Figure 4 shows how the warp parameter varies as a function of radius and time in both simulations. One way to view this pair of figures is to focus on behavior as a function of time at a fixed radius. From this perspective, we see that $\hat{\psi}$ oscillates between quite small and $\simeq 2.5$ on timescales of order a fiducial orbit. In other words, the warp induced by the

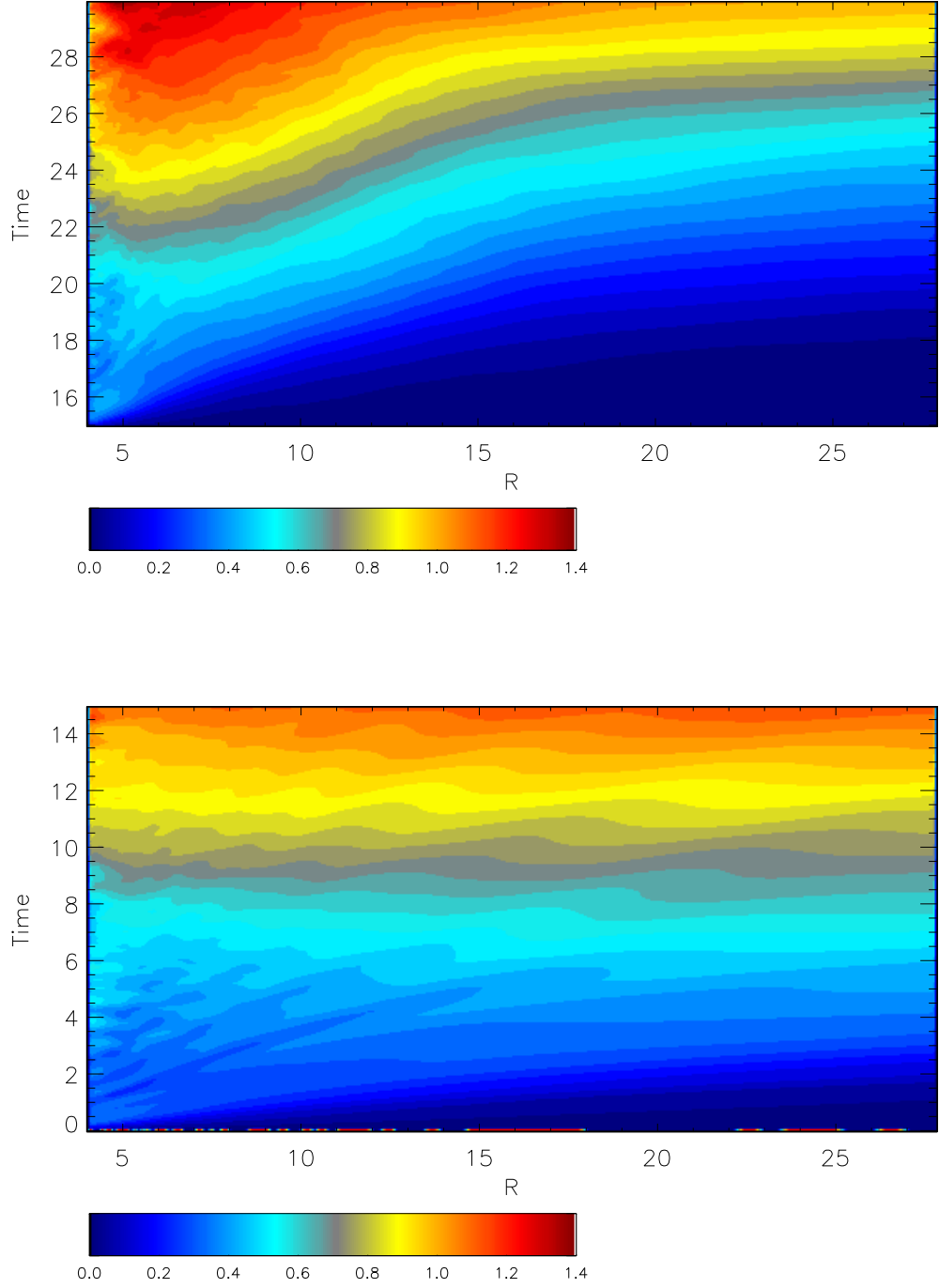


Fig. 3.— Color contours (see color bar) of precession angle in units of π as a function of radius and time. Upper panel is BP-m; lower panel is BP-h.

radially-varying external torque appears to exhibit a “stick-slip” behavior: the differential torquing builds the warp until $\hat{\psi}$ reaches this maximum value, and then the strong radial flows associated with such a nonlinear warp rapidly erase it. The warp grows larger at the outside of the disk, where the surface density is small. It is also noteworthy that the “stick-slip” oscillation is considerably more sharply defined in the HD case than in the MHD case; this is not surprising in view of the turbulence that is the hallmark of the latter, but nonexistent in the former.

The locations of strong warping propagate coherently outward over time. Although the correspondence is not perfect, the trajectory of the first and strongest pulse in both simulations is close to what would be expected for a bending wave. The time-width of this pulse defines a characteristic frequency, $\omega_* \sim 2$ radians per fiducial period. Bending waves more than a few times greater than the local precession frequency travel at half the local isothermal sound speed; bending waves with lower frequencies travel more slowly, becoming non-propagating when their frequency drops below the local precession frequency (Lubow et al. 2002). Because the precession frequency reaches ω_* only for $r \lesssim 7$ and decreases rapidly outward ($\propto r^{-3}$), the asymptotic wave speed applies to most of the mode content for these pulses for all radii $\gtrsim 7$. We plot tracks defined by this speed in Figure 4, where it appears to provide a reasonable approximation to the propagation of the first pulse in both BP-m and BP-h. That the first pulse in BP-h spreads slowly with radius indicates a spread in propagation speeds, suggesting the presence of wave components with frequencies ranging down from ω_* to $\gtrsim \omega(r)$.

In BP-h, but not in BP-m, there is also a rough correlation between the trajectory of that first pulse and the establishment of approximately solid-body precession. A clue to the origin of this contrasting behavior may be found in the much more irregular variation of warp magnitude along the trajectory of the pulse in BP-m than in BP-h. We suggest that the turbulence permeating the disk in BP-m disrupts smooth propagation of such a wave: the ratio $(\langle v_{Ar}v_{A\phi} \rangle / c_s^2)^{1/2} \simeq 0.2\text{--}0.3$ (the average is over spherical shells) immediately before the torques begin (here $v_{A(r,\phi)} \equiv B_{(r,\phi)} / \sqrt{4\pi\rho}$). Laminar magnetic field would probably be less effective in interfering with a bending wave because the magnetic tension on such long length scales (vertical wavelength $\simeq 2H$) is relatively weak; for example, the growth rate of an MRI mode with the vertical wavelength of the bending wave is only $\sim \Omega/7$. That solid-body precession is never quite achieved in BP-m will prove crucial in our analysis of the contrasting alignment behavior shown by these two simulations.

Later $\hat{\psi}$ pulses, however, propagate substantially more slowly and decelerate outward. In fact, their speeds decrease steadily from each late pulse to the next. These observations suggest that these pulses are not driven by bending wave dynamics. As we have just seen, the

speeds of bending waves are controlled by the isothermal sound speed and the relationship between their frequency and the local precession frequency. Neither the sound speed nor the local precession frequency is a function of time, while the time-dependence of the pulse widths suggests that ω_* increases slowly. Thus, the speeds of bending waves should vary little with time or possibly become even closer to the asymptotic value of half the isothermal sound speed, whereas the speeds of these pulses become progressively slower and slower at later times. Instead, the later pulses appear to be better described by differential precession twisting the disk from flat to a critical value of $\hat{\psi}$. In this essentially kinematic picture, the disk begins in a state in which it is locally flat (more precisely, it is flat near radius r at time $t_0(r)$). The differential torques then build a warp without (at first) any coupling between adjacent rings of gas. Once the warp grows to the point at which $\hat{\psi} = \hat{\psi}_{\text{crit}}$, neighboring rings couple through radial flows and, after about one local orbit, that region of the disk is once again flat. In this picture, the radius r_{crit} at which $\hat{\psi} = \hat{\psi}_{\text{crit}}$ moves outward in time according to

$$r_{\text{crit}} = r_M \left\{ \frac{6\pi}{H/r} \frac{\omega(r_M) \sin \beta}{\Omega(r_M) \hat{\psi}_{\text{crit}}} [t - t_0(r)] \right\}^{1/3}, \quad (5)$$

where β is the angle between the orbital axis and the central mass’s spin-axis, and time is measured in fiducial periods (orbital periods at r_M). The dotted curve in Figure 4 assumes $\hat{\psi}_{\text{crit}} \simeq 2.5$, consistent with the most common value of $\hat{\psi}$ along these ridgelines and sets $t_0(r)$ to one local orbit after the peak warp induced by the bending wave passes that radius. The delay of one orbit is a rough approximation to the time required for warp relaxation from a $\hat{\psi}$ of that magnitude (Sorathia et al. 2013). In both cases, but especially for BP-h, this model does a fairly good job of reproducing the track followed by the second major pulse in $\hat{\psi}$. It appears, therefore, that although the twist induced by the differential torques is initially propagated outward by a bending wave, subsequent twists—which also have considerably smaller amplitude—propagate purely kinematically.

3.3. Alignment

Figure 5 shows the alignment angle β (in units of π) in the two simulations as a function of radius and time. Alignment is the respect in which MHD makes the greatest difference. For the first several orbits, BP-h aligns significantly more quickly than BP-m at large radii, while at small radii the opposite is true. At later times, however, alignment virtually stops in BP-h, while continuing steadily in BP-m. As a result, whereas half the initial alignment at $r = 7$ has been eliminated after $\simeq 5$ orbits in BP-m, that degree of alignment is not achieved even by the end of 15 orbits in BP-h; BP-h diminishes its misalignment by $\simeq 40\%$ at $6 < r < 9$ by $\simeq 4$ orbits, and then ceases to change alignment thereafter. By contrast, the

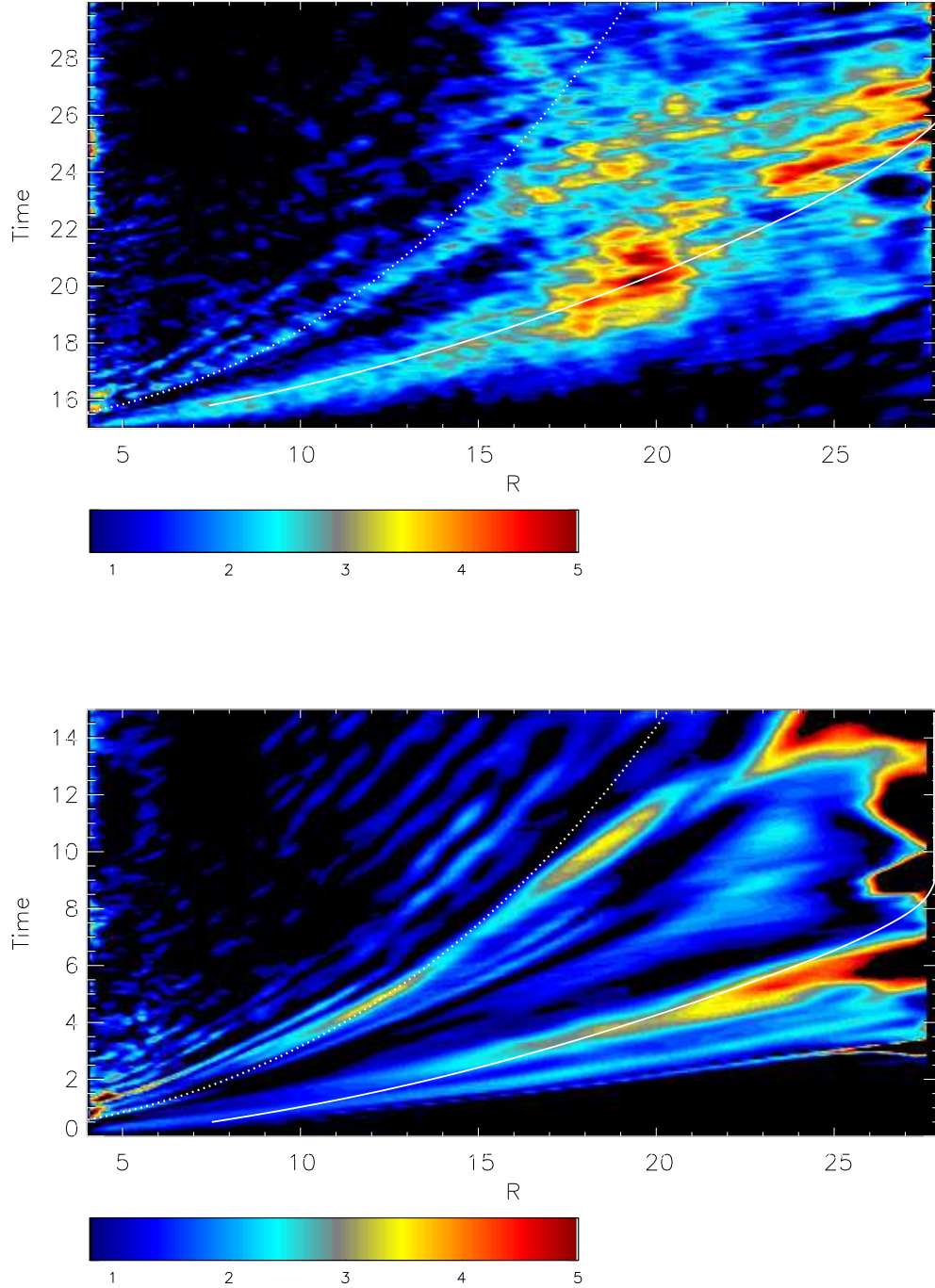


Fig. 4.— Color contours (see color bar) of $\hat{\psi}$. Upper panel is BP-m; lower panel is BP-h. The color scale goes to black for $\hat{\psi} \leq 0.8$ in order to emphasize the boundary between linear and nonlinear warps. In each panel, there are two superposed white curves. The solid one represents the trajectory of a bending wave (with speed one half the mass-weighted isothermal sound speed: Lubow et al. (2002)), the dotted one shows the trajectory implied by eqn. 5 with $t_0(r)$ as described in the text.

entire range of radii interior to $r \simeq 15$ in BP-m has diminished its misalignment by at least half by the end of its 15 orbits, and the misalignment has been sanded down to $< 0.02\pi$ for all $r < 11$.

Comparison of Figures 5 and 4 also shows a close correspondence between the regions where the inclination angle has been reduced to less than $\simeq H/r$ and regions where the warp is always in the linear regime. This is, of course, a natural consequence of the fact that when the inclination is $< H/r$, there cannot be radial contrasts in inclination or orientation any larger than that. What is more noteworthy about this region of permanently linear warp is that it is also the region where the inclination in BP-m continues to decline, whereas no such improvement in alignment occurs in BP-h. We will return to this point later.

3.4. MHD vs. HD

As we have already pointed out, at least through the initial stages of alignment, MHD effects appear to be secondary to hydrodynamic effects, although the sense of that secondary contribution is to promote alignment. The data shown in Figure 6 illustrate explicitly the relative importance of magnetic and pressure forces. The disk curves up and down in these coordinates because at this radius and time it has already moved out of the equatorial plane of the grid. Compared at the same location during the time when the disk is aligning most rapidly, the radial gas pressure gradient is generally ~ 10 – 100 times larger than the radial magnetic pressure gradient, while the radial magnetic pressure gradient is ~ 3 – 10 times larger than the total magnetic tension force. At later times, the magnetic forces rise relative to the fluid forces, but only by a factor of 2–3. Thus, in terms of instantaneous forces, magnetic effects are always considerably weaker than hydrodynamic forces.

The relative weakness of magnetic forces is enhanced by the fact that after the torque begins, the total magnetic energy in the disk declines sharply, falling by about a factor of 2 over the first 5 orbits of torque. From then until the end of the simulation, the total magnetic energy varies hardly at all. It is possible that some of the field loss is a numerical artifact, caused by a combination of newly-created flows oblique to the coordinate grid and an artificially large rate of magnetic reconnection as the radial flows driven by the disk warps push regions of oppositely-directed field toward one another. However, we believe that it is not entirely artificial. We have several reasons to think so. The first is that the degree of obliquity is never terribly large: an inclination of 12° is not very great, and the numerical diffusion experiments of Sorathia et al. (2013) found that even with a grid a factor of 4 coarser than ours, only $\simeq 0.5\%$ of the angular momentum was lost after 10 orbits of integration at a slightly greater inclination (15°). The second is that before carrying out

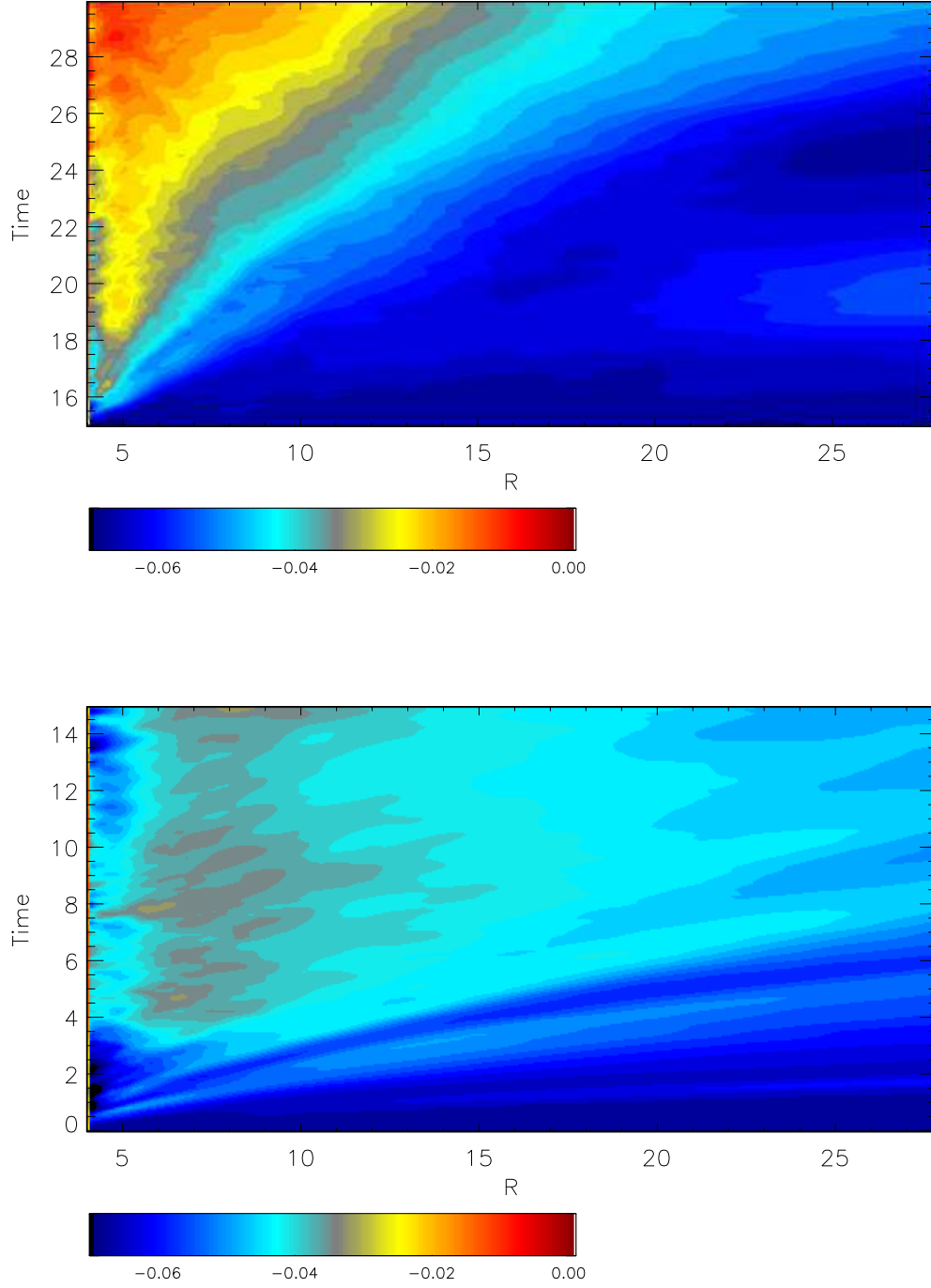


Fig. 5.— Color contours (see color bar) of the inclination angle (in units of π) as a function of radius and time. Upper panel is BP-m; lower panel is BP-h.

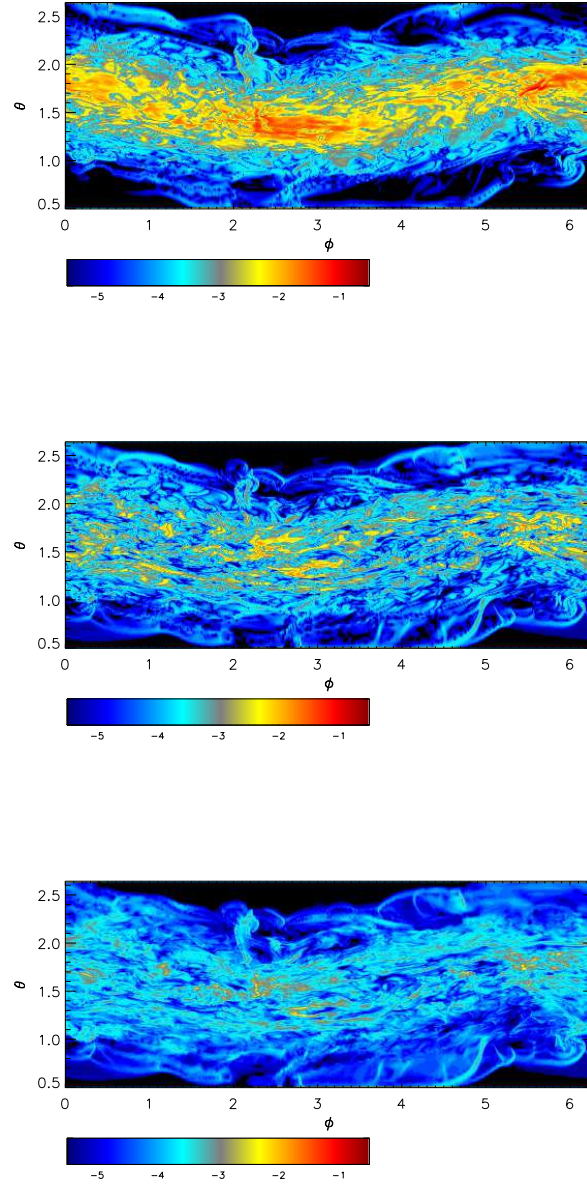


Fig. 6.— Color contours on a logarithmic scale of the magnitudes of three force densities: the radial component of the gas pressure gradient (top panel), the radial component of the magnetic pressure gradient (middle panel), and the total magnetic tension (bottom panel). All are measured as a function of ϕ and θ on the $r = 10$ shell at 4 orbits after the torque was turned on in BP-m.

BP-m, we ran the same problem on a grid a factor of 2 coarser in each dimension. The magnetic energy loss after the initiation of the torque in that run was larger, but not by much, a factor of 3 decrease rather than a factor of 2. The third reason is that the radial flows, which sometimes lead to shocks, do contain regions where reconnection is driven by the fluid motions; in these cases, the local rate of reconnection may be resolution-dependent, but its end-result is not. Thus, some of the field loss we see is likely due to lack of resolution, but it probably does not account for the entire effect. It is also possible that the development of the magneto-rotational instability is altered in the presence of a warp.

Thus, although our simulation includes a full treatment of MHD turbulence, it turns out to have a relatively small effect on the magnitude of the radial flows primarily responsible for transporting misaligned angular momentum through the disk. The situation in even a magnetized disk in fact resembles quite closely that explored in Sorathia et al. (2013), in which the relaxation of disk warps in a purely hydrodynamic context was studied. Just as was found in that paper, we find that when $\hat{\psi} > 1$, which is the generic situation when there is any substantial inclination, the magnitudes of these radial flows are primarily controlled by the fluid dynamics of order unity pressure contrasts in an orbital setting, i.e., quasi-free expansion limited by orbital mechanics.

Despite the dominance of hydrodynamic effects over magnetohydrodynamic effects in most aspects of warped disk evolution, we have also seen that MHD appears both to accelerate alignment and to continue it longer. It is noteworthy that the purely hydrodynamic disk ceases alignment progress when its inclination reaches $\simeq 6^\circ$, here one scale-height (Fig. 5b). At that point (see also Fig. 4b), it becomes almost impossible for any warps to reach nonlinear amplitude. Consequently, the Reynolds stress responsible for radial mixing of unaligned angular momentum drops rapidly because it is a strongly increasing function of $\hat{\psi}$ when $\hat{\psi} \simeq 1$ (Sorathia et al. 2013). On the other hand, when MHD effects are present, the turbulence they cause creates much short lengthscale structure in the velocity field, enhancing the angular momentum mixing rate. This mixing rate is considerably faster than the inflow rate associated with Reynolds stresses in a flat disk because the scale of the gradients is much smaller: $\sim 0.1r$ rather than $\sim r$.

We close this section with an examination of an assumption frequently made in other studies of warped disks: that the vertical shear of radial motions induces a stress that can be phenomenologically modeled as an isotropic “ α viscosity” (Papaloizou & Pringle 1983). Such a viscosity would create a viscous stress proportional to the shear (but, of course, with opposite sign) whose magnitude is $\sim \alpha p$ when $\partial v_r / \partial z \sim \Omega$. Some support was given to this hypothesis by Torkelsson et al. (2000), who measured the decay of epicyclic motions in a numerical simulation of a vertically-stratified shearing box with MHD turbulence, although

their conclusions were somewhat clouded by the limitations of their approximations and by their finding that larger amplitude motions were primarily damped by a different mechanism, the excitation of inertial waves.

Here we test a form of this hypothesis: that the Maxwell stress of MHD turbulence (whose r - ϕ component is responsible for accretion) acts in the same manner independent of the orientation of the shear. In this context, the relevant component of the Maxwell stress is r - θ . We therefore compute the ratio

$$\alpha_* = \frac{B_r B_\theta \Omega}{4\pi p \partial v_r / \partial z} \quad (6)$$

on a sample spherical shell when alignment is beginning at that location.¹ If the isotropic α viscosity hypothesis were true, α_* would be consistently positive and have magnitude ~ 0.01 – 0.1 , similar to the ratio of the time-averaged and vertically-integrated r - ϕ component of the magnetic stress to the similarly averaged and integrated pressure. As Figure 7 demonstrates quite clearly, neither of these expectations is confirmed. The quantity α_* is equally likely to be positive or negative, and its absolute magnitude in the disk body—including where the shear and Reynolds stress are greatest—is generally $\sim 10^{-5}$ – 10^{-4} . The mass-weighted mean $\langle \alpha_* \rangle \simeq 3 \times 10^{-5}$. When averaged over snapshots spanning 0.3–1 fiducial orbit (which is also the local orbital period for the data shown in Fig. 7), the magnitude of the shear decreases, but the radial pressure gradients induced by the warp preserve some overall consistency. Consequently, the shear diminishes only somewhat when averaged over short time intervals. On the other hand, time-averaging over even as brief a time as half a fiducial orbit (five snapshots) reduces the magnitude of the r - z magnetic stress by almost an order of magnitude.

To quantitatively calibrate the measured magnitude of α_* , we note that the rms magnitude of the r - z shear is $\simeq 2.6\Omega$ when weighted by mass and $\simeq 6.9\Omega$ when weighted by volume. A further sense of scale may be gleaned from the fact that both the r - r and the r - z components of the Reynolds stress are frequently $\sim (1$ – $10)p$ (and the r - z Reynolds stress has no more correlation with the corresponding shear than the same component of the Maxwell stress). In other words, the radial flow speeds are generally transonic, the lengthscale of vertical variation is several times smaller than the pressure scale height (i.e., turbulence is important), and the overall dynamics are dominated by pressure gradients and gravity, with only small contributions from any other sources of stress.

¹Because of the disk’s warp and twist, the θ -direction is exactly normal to the disk only at large radii where there has been little precession or alignment. However, the relatively small initial misalignment angle (12°) means the error due to imprecise identification of the disk normal is quite small compared to the magnitude of the effect we measure.

As a final comment, it is worth noting that in several respects this result can be understood on the basis of qualitative arguments. First, it is not surprising that the r - z component of Maxwell stress should be much smaller in magnitude than the r - ϕ component when the magnetic fields are associated with MRI-driven turbulence. Simulations of MRI-driven turbulence in flat disks have consistently found that $|B_\phi| \sim 3|B_r| \sim 10|B_z|$ (Hawley et al. 1995; Stone et al. 1996; Hawley et al. 2011); even without allowance for the degree of correlation between these components, one would therefore expect the r - z component to be an order of magnitude smaller than the r - ϕ component. Because the consistency of orbital shear imposes a strong correlation between B_r and B_ϕ , yet r - z shear has no consistent value, one might also expect that the degree of correlation in r - z would be much weaker than in r - ϕ . The lack of sign correlation can also be understood intuitively. Magnetic stresses in conducting fluids result from *strain* in the fluid, not shear. If the flow is oscillatory, strain is $\pi/2$ different in phase from shear, and such a phase offset would entirely eliminate any sign correlation. Fluctuations due to turbulence further diminish any direct tie between magnetic stress and fluid shear.

4. Analysis

4.1. The alignment rate

To understand these results, it is helpful to frame them in terms of the global angular momentum budget. Alignment is often described as due to “dissipation” associated with angular momentum diffusion (Papaloizou & Pringle 1983). However, this description is a bit imprecise. Changing the direction of an angular momentum first and foremost requires a torque. The mechanism producing this torque may or may not be dissipative, and any dissipation involved may or may not be associated with a process described by a classical diffusion equation. What is truly essential is that new angular momentum introduced into the system must be brought to a location where it can cancel the misaligned angular momentum. More specifically, there are only three ways the angular momentum of a given disk region can change: by a divergence of Reynolds stress, a divergence of Maxwell stress, and an external torque. However, the Lense-Thirring torque by its very nature cannot change $|\mathbf{L}_\perp|$ at the location where the torque is exerted because it is always exactly perpendicular in direction. It follows that to align a ring at radius r , there must be a way to bring its angular momentum from a region with a precession phase *different* from that of radius r , where the Lense-Thirring torque has a component opposite in direction to $\mathbf{L}_\perp(r)$. It is possible for diffusive mixing to accomplish this, but it can also be accomplished by other means, and any mixing process must satisfy certain specific conditions. The region that is mixed must

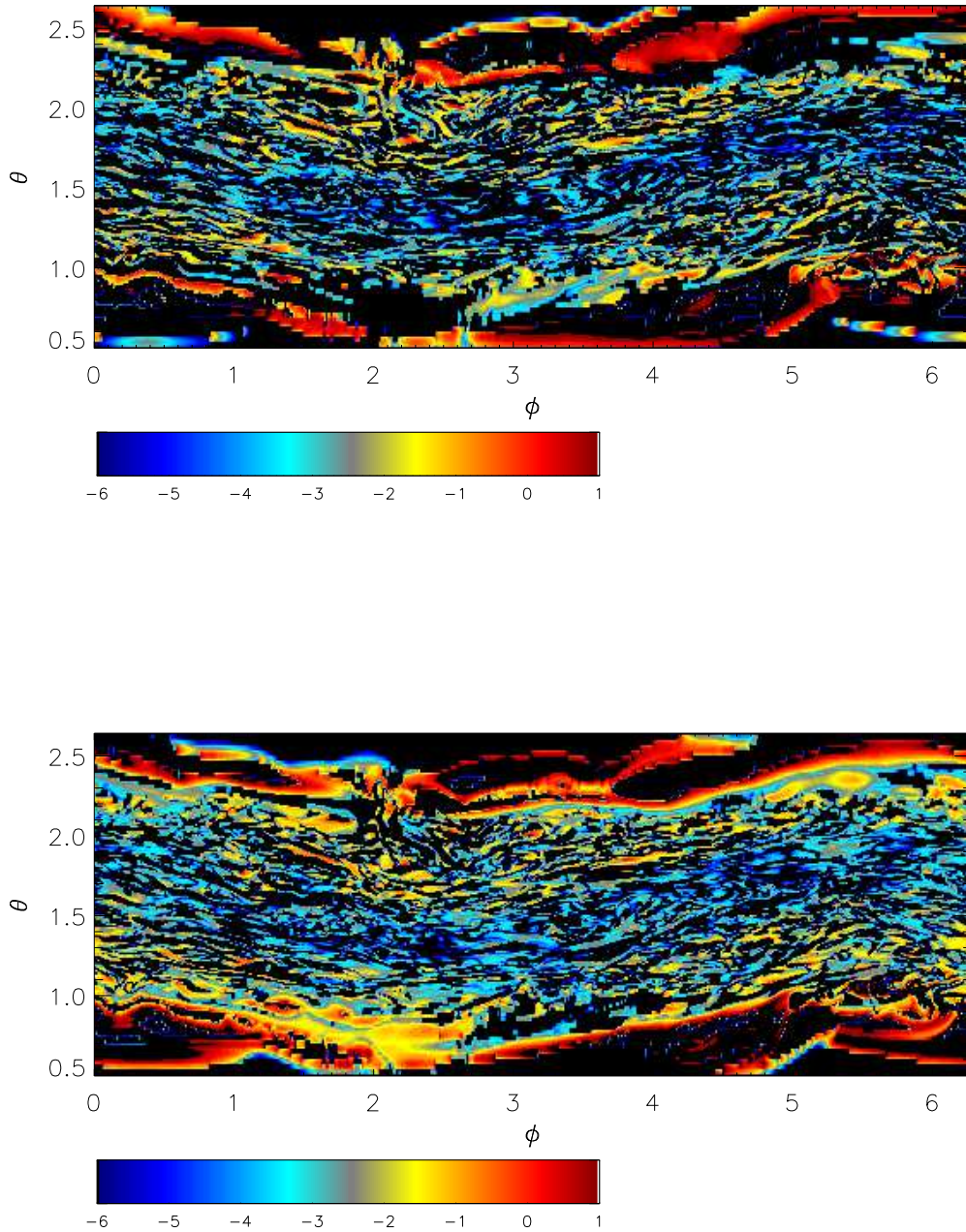


Fig. 7.— Color contours (see color bar) of $\log_{10}(|\alpha_*|)$ as defined in text, measured on the same spherical shell and at the same time in BP-m as in Fig. 6. In order to display these quantities on a logarithmic scale, we separate the data into two cases: where $\alpha_* > 0$ (upper panel) and where $\alpha_* < 0$ (lower panel). Black indicates a region where α_* has the opposite sign from the colored data in that panel.

contain a large enough range of precession phase that some portion of it has a torque with a direction that can cancel $\mathbf{L}_\perp(r)$, but not so large that mixing leads to complete cancellation in the net torque. In addition, as we have already seen, magnetic forces are in general quite small compared to hydrodynamic forces, so the Maxwell stress contributes little to the alignment. Consequently, alignment must be due to divergences in the Reynolds stress. Moreover, because the interesting gradients are all in the radial direction, it makes sense to think only about radial angular momentum flows.

More formally, we define the radial angular momentum flux as

$$S_{r,(x,y,\perp)} \equiv r^2 \int d\theta \sin \theta \int d\phi \rho v_r \ell_{(x,y,\perp)}, \quad (7)$$

where $\ell_{x,y,\perp}$ is the local specific angular momentum in the x , y , or perpendicular (i.e., combining x and y) direction. The magnitudes of these fluxes are shown in Figures 8 and 9. The global shape of the radius and time dependence of the fluxes is similar in the two simulations, and in units of shell-integrated $\rho r v_{\text{orb}}^2$, the magnitudes of the fluxes in both simulations are similar to those seen in Sorathia et al. (2013) when $\hat{\psi} \simeq 1$. In that previous paper, fluxes of this magnitude led to approximate disk flattening on orbital timescales; much the same result is seen in both of these new simulations.

However, there are also significant contrasts. Most importantly, in the hydrodynamic case, but not in the MHD simulation, there is a sequence of three large amplitude flux pulses of alternating sign. The first two are due to a transient in which the hydrodynamic disk relaxes from its initial state, which is not exactly in equilibrium; their effects nearly cancel. The third, although smaller in magnitude, is in the long-run more significant. It follows the track already seen in Figure 4 that we interpreted as a bending wave. This track also corresponds to the flattening of the disk seen in Figure 3 and coincides with the last stage of alignment seen in Figure 5. In other words, it appears that this bending wave pulse effectively flattens the hydrodynamic disk, so that it precesses very nearly as a solid-body thereafter. Once the bending wave has passed, BP-h maintains a generally higher level of outward angular momentum flux than found in BP-m because it remains misaligned to a greater degree at small radius where the torques operate (see also Figs. 1 and 2). By contrast, in BP-m, although there is an initial bending wave, it is partially disrupted, and is much less effective at flattening the disk, as demonstrated also by the generally higher levels of $\hat{\psi}$ seen in the MHD panel of Figure 4 between the tracks of the bending wave and the kinematic precession pulse.

To gain a sense of scale, it is also useful to look at a normalized version of the angular momentum flux,

$$\hat{S}_{r\perp} \equiv \frac{|S_{r\perp}|}{c_s \partial L_\perp / \partial r}. \quad (8)$$

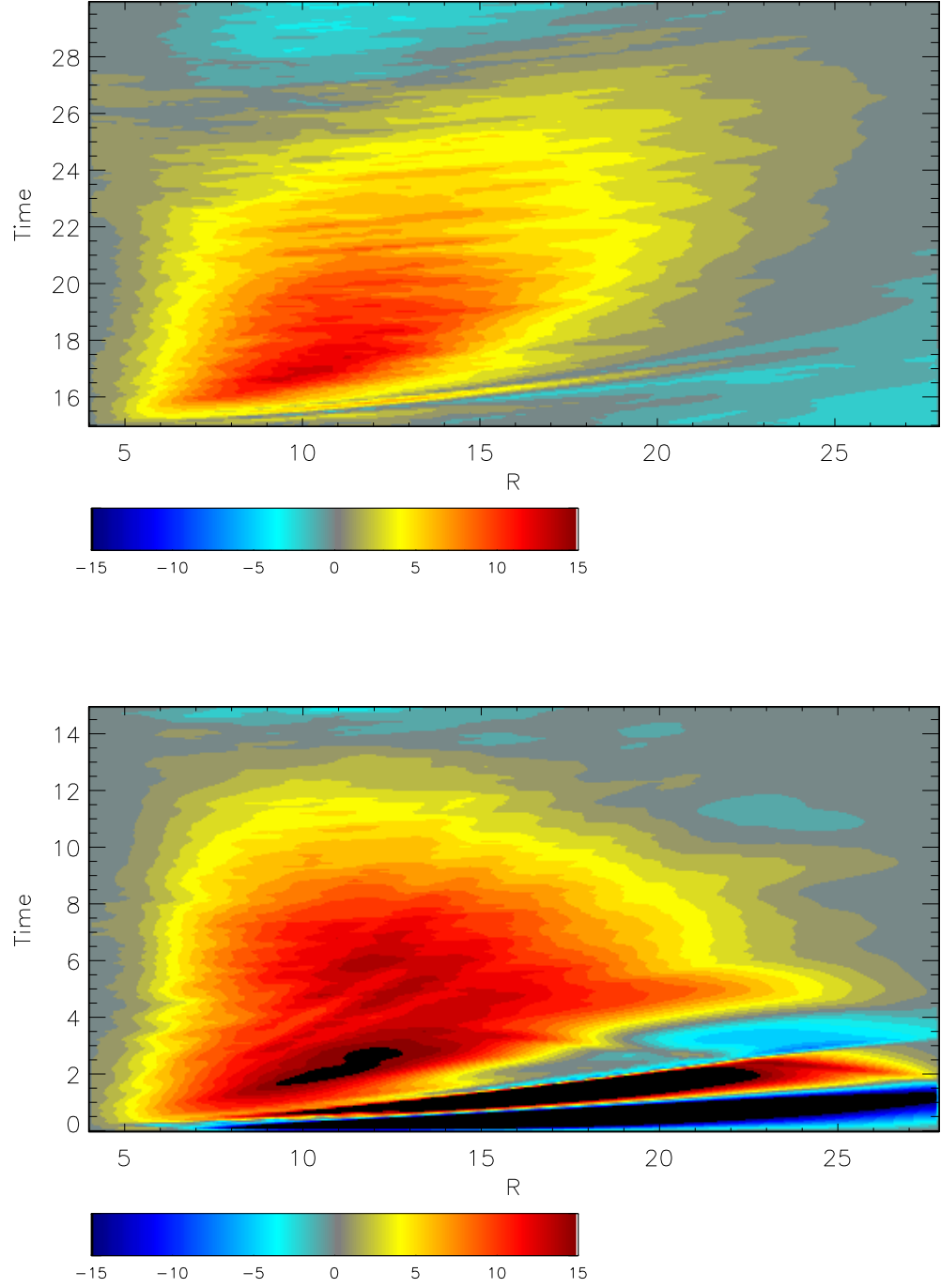


Fig. 8.— Color contours (see color bar) of the radial flux of the x component of angular momentum. Upper panel is BP-m; lower panel is BP-h.

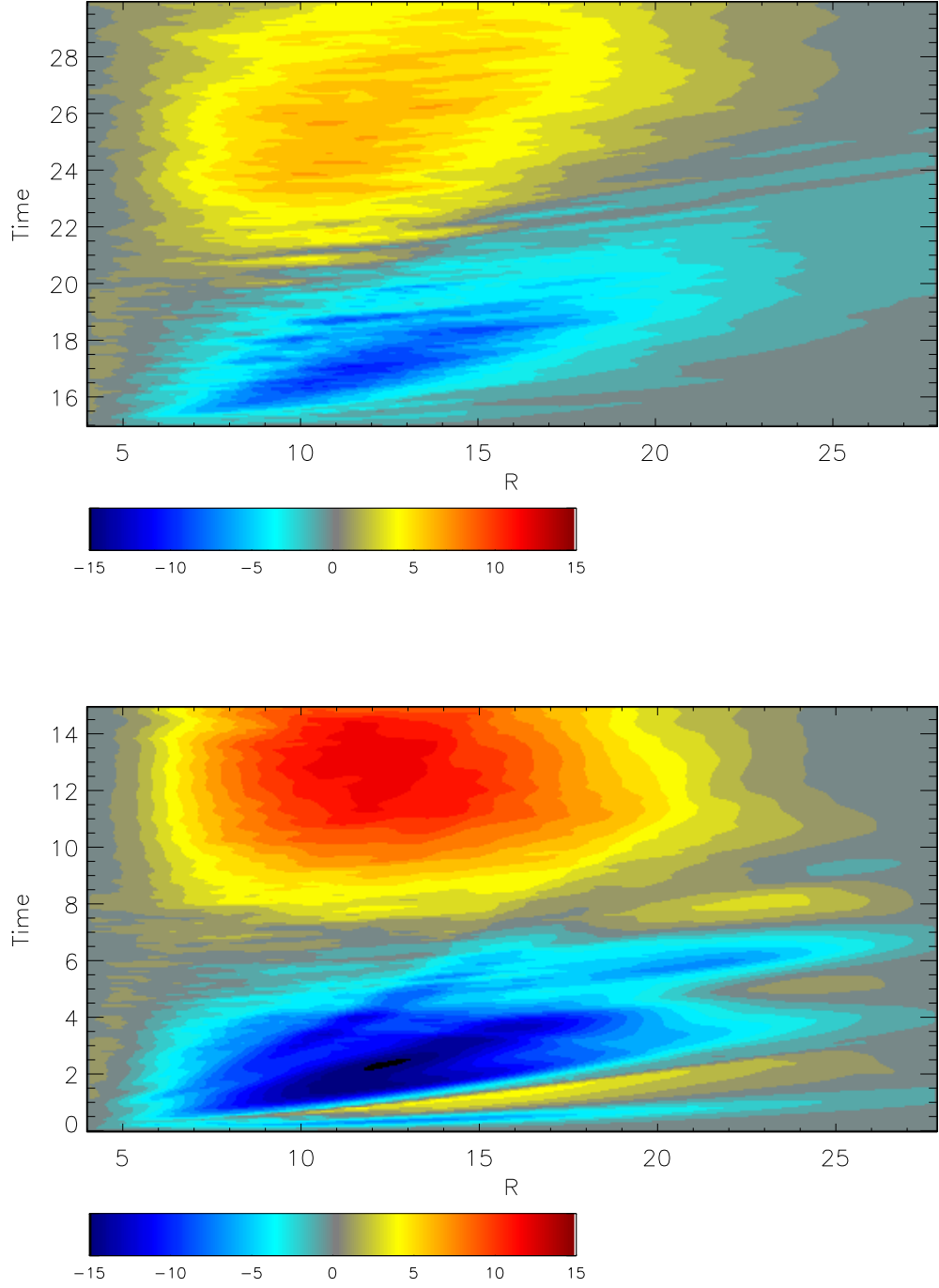


Fig. 9.— Color contours (see color bar) of the radial flux of the y component of angular momentum. Upper panel is BP-m; lower panel is BP-h.

This quantity captures the efficiency with which local fluid is able to pass along its angular momentum. Shown in Figure 10, we see that this quantity is typically a few tenths; that is, if the mean flow rate is exactly the sound speed, the flux carries $\sim 15\text{--}30\%$ of the local angular momentum. Although the absolute level of the fluxes in the MHD case was always somewhat smaller than in the HD case, $\hat{S}_{r\perp}$ is always larger in MHD. In other words, the MHD case puts more of its available misaligned angular momentum into motion. The contrast is especially noticeable in locations where the swing into alignment is most rapidly taking place. On this basis, it might be reasonable to identify the magnitude of $\hat{S}_{r\perp}$ found here with $h/\Delta r$, where Δr is the radial scale of the warp. We caution, however, that, as shown by Sorathia et al. (2013), the actual functional relationship between $S_{r\perp}$ and the warp magnitude $\hat{\psi}$ is nonlinear, exhibits time delays, and also depends on the global character of the warp. Consistent with those results, $\hat{S}_{r\perp}$ varies by a factor ~ 2 , both as a function of time and as a function of radius. Because $\hat{S}_{r\perp}$ is proportional to the ratio of angular momentum flux to the radial gradient of angular momentum direction, these fluctuations support the conclusion of our previous paper that simple diffusion model does not fully describe the behavior of this system.

The next step in our inquiry is to examine the effect of divergence in the angular momentum flux. Comparing Figures 8 and 9 with their torque counterparts (Figs. 1 and 2, respectively), it is apparent that the fluxes are largest at radii considerably greater than where the torques are largest. In other words, the angular momentum delivered at small radii by the torques is collected and swept outward. Beyond $r \simeq 14\text{--}17$, where the fluxes peak, the transported angular momentum is deposited, a bit like silt dropping out of a slowing river. The distribution of the net rate of change in angular momentum can be seen in Figures 11 and 12. Both the initial bending wave and the later, slower pulses seen in Figure 4 can be discerned in the HD panel of Figure 11. These pulse trains are much less apparent in the MHD case. One fact uniting the HD and MHD plots of Figures 11 and 12, however, is that in both cases the net rate of change in angular momentum in regions where the rate of angular momentum delivery by torque is high is in fact quite small. In other words, where the torque is delivered, increased outward angular momentum flux removes the great majority of it and transports it outward. This is why the local precession rate in the inner disk is substantially smaller than the test-particle model would predict and also why, especially in BP-m, much of that angular momentum is used for alignment rather than precession.

The effects shown in Figures 11 and 12 can be summarized by the fact that

$$\frac{\partial^2 L_{\perp}}{\partial r \partial t} = -\frac{\partial L_x}{\partial r} \frac{\partial S_{rx}}{\partial r} - \frac{\partial L_y}{\partial r} \frac{\partial S_{ry}}{\partial r}. \quad (9)$$

If the ratio $(\partial S_{rx}/\partial r)/(\partial S_{ry}/\partial r)$ were equal to G_x/G_y , the perpendicular angular momentum would not change at all because that is the condition for precession. However, the ratio of the

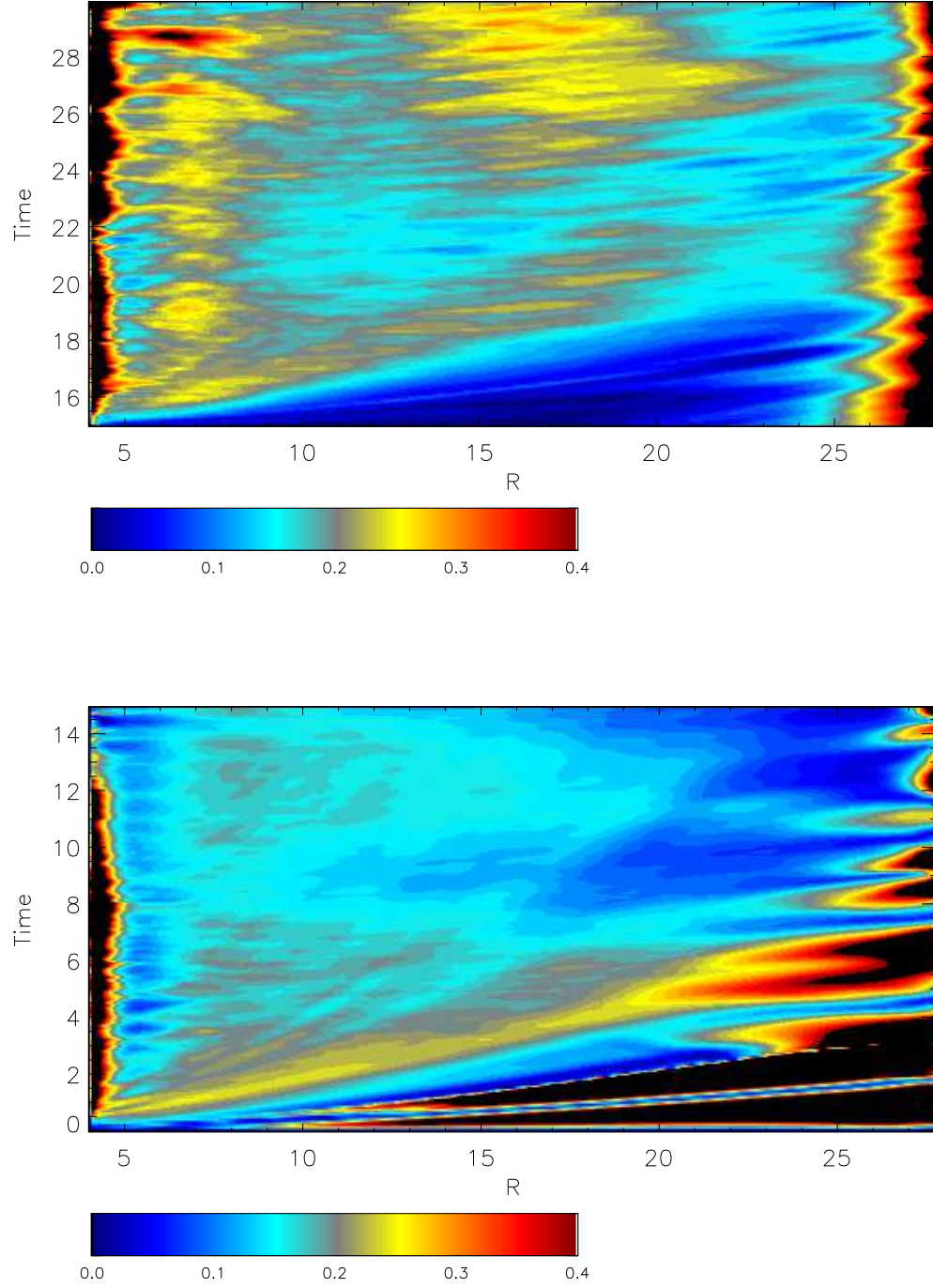


Fig. 10.— Color contours (see color bar) of $\hat{S}_{r\perp}$, the normalized radial flux of the perpendicular component of angular momentum. Upper panel is BP-m; lower panel is BP-h.

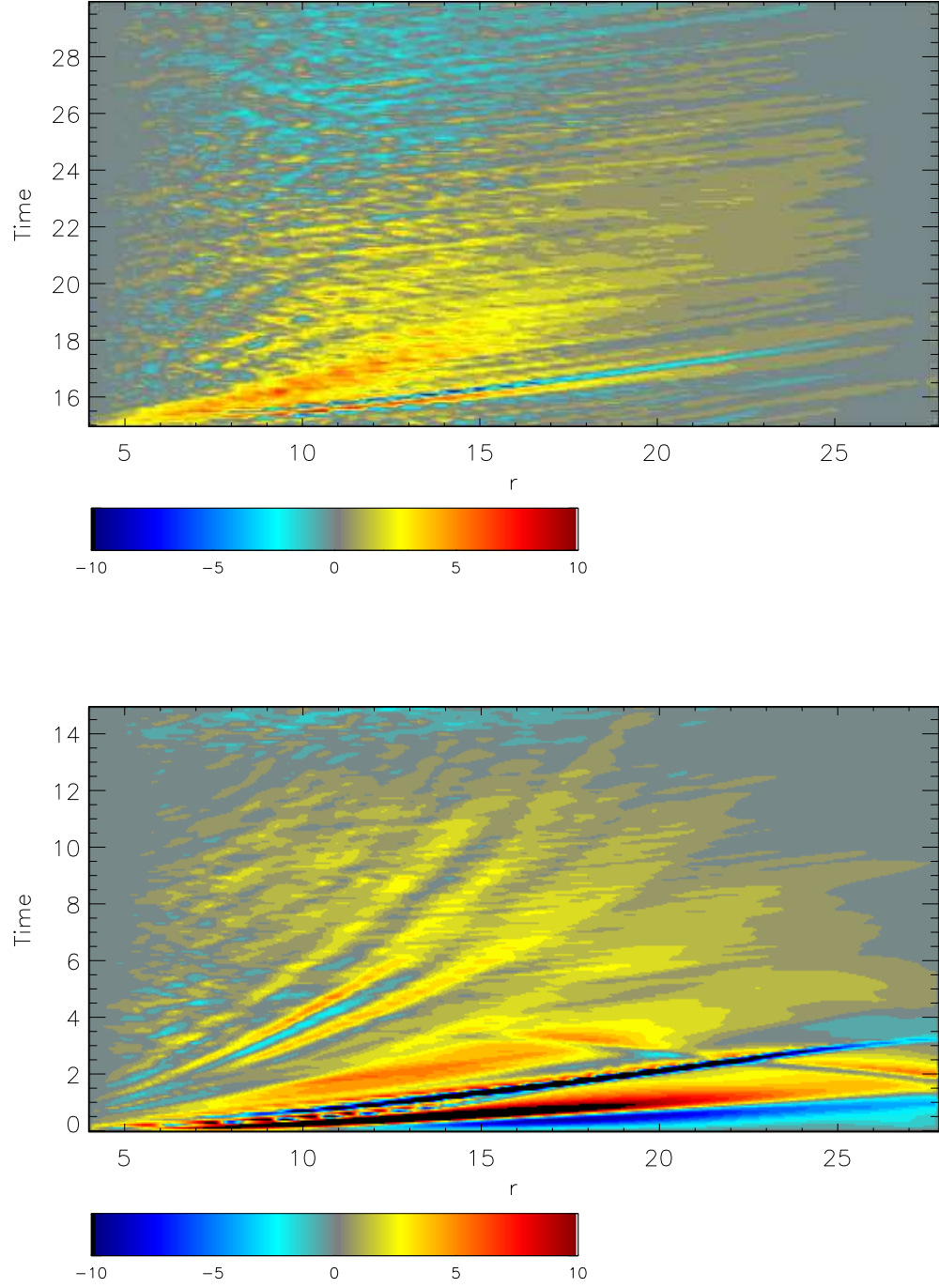


Fig. 11.— Color contours (see color bar) of the net rate of change per unit time in the x component of angular momentum in each radial shell. Upper panel is BP-m; lower panel is BP-h.

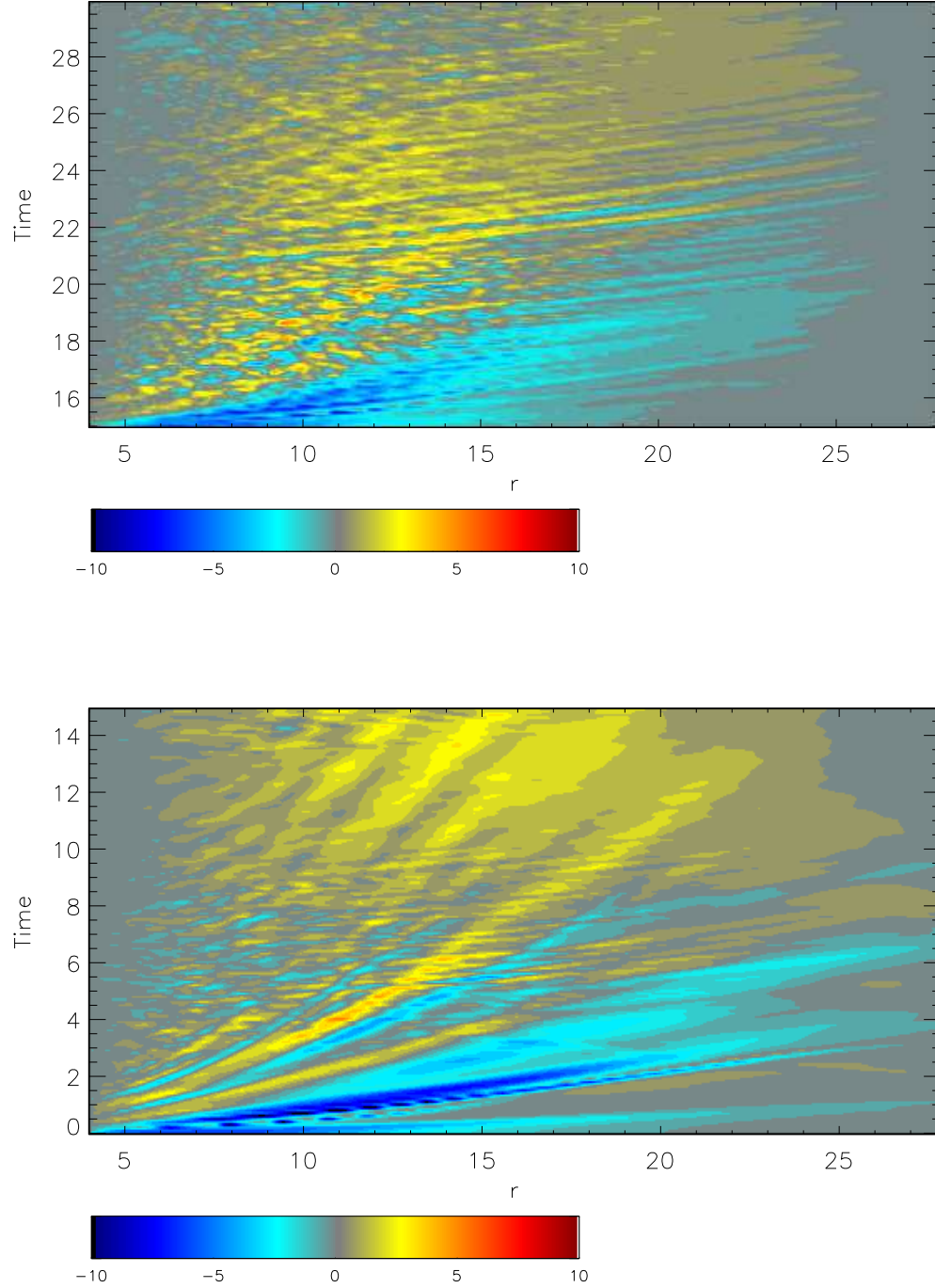


Fig. 12.— Color contours (see color bar) of the net rate of change per unit time in the y component of angular momentum in each radial shell. Upper panel is BP-m; lower panel is BP-h.

angular momentum deposition rates in the x and y directions does not necessarily match the ratio required for precession at that location. To accomplish alignment, all that is required is for

$$\frac{\partial S_{sry}/\partial r}{\partial S_{rx}/\partial r} < -\frac{\partial L_x/\partial r}{\partial L_y/\partial r}, \quad (10)$$

where the RHS is the exact precession ratio. Alignment proceeds most rapidly where this inequality is most strongly satisfied.

Another way of putting the same point is to observe that alignment is achieved most efficiently when the vector

$$\frac{\partial^2 \mathbf{L}_\perp}{\partial r \partial t} = -\frac{\partial S_{rx}}{\partial r} \hat{x} - \frac{\partial S_{ry}}{\partial r} \hat{y} \quad (11)$$

is exactly anti-parallel to $\partial \mathbf{L}_\perp / \partial r$. In principle the angle γ between $-\partial \mathbf{L}_\perp / \partial r$ and the rate at which it is changed might be anywhere from 0 to π . The angle optimally efficient for alignment is 0; the angle that produces pure precession is $\pi/2$. In both BP-h and BP-m, we find that during times of alignment $\langle \cos \gamma \rangle \simeq 0.5$ although there are sizable fluctuations around this value at specific times and locations. On the other hand, $\langle \cos \gamma \rangle$ decreases over time in BP-h from approximately this value during the first $\simeq 6$ orbits to close to zero during the remainder of the simulation.

In large part, the angle γ is determined by the relative precession angles of the region where the torque occurs, which supplies the angular momentum for the outward flux, and the region where the angular momentum is deposited. For maximal alignment rate, the direction of the deposited angular momentum should be the direction of the torque exerted when the precession angle is $\pi/2$ in advance of the local precession angle. The value of $\langle \cos \gamma \rangle$ seen in BP-m indicates a precession angle difference closer to $\simeq \pi/6$ than $\pi/2$, but there is nonetheless sufficient offset to drive alignment. During early times in BP-h the situation is similar. At late times in BP-h however, $\langle \cos \gamma \rangle \simeq 0$ because the disk orientation is very nearly the same at all radii, and the time required to transport angular momentum from the small radii where the torques operate to larger radii is short compared to the solid-body precession period. In other words, having at least some warp in the disk is essential to alignment.

The detailed radial and time dependence of the net rate of change of misaligned angular momentum $\partial^2 L_\perp / \partial r \partial t$ in BP-m is shown in Figure 13. Several things stand out in this plot. One is that the local rate of change of misaligned angular momentum is predominantly, but not exclusively, negative. That is, there are frequently moments when an individual ring becomes *less*, not *more* aligned, even though the long-term trend is toward alignment. Another point is that, not surprisingly, the largest part of the change in angular momentum is associated with the range of radii ($8 \lesssim r \lesssim 15$) with the greatest mass and therefore the

greatest amount of misaligned angular momentum to change.

Perhaps more surprisingly, this figure is also marked by a large number of streaks indicating rapid outward motion. The white curve in the figure follows the path of an adiabatic sound wave directed radially outward. The very close correspondence between its slope in this diagram and the slopes of the streaks demonstrates clearly that these are the traces of sound waves. Although they are certainly not regular, there is a typical time interval between these waves, $\simeq 0.5$ fiducial orbits.

In BP-m, alignment is achieved beginning at small radii. Consequently, one can speak of the outward motion of an alignment front. On dimensional grounds, one might estimate the rate at which this front moves outward by the ratio of the rate at which unaligned angular momentum is given to the disk by torque to the magnitude of the local angular momentum requiring alignment. However, as the previous discussion would suggest, this estimate should be corrected by a factor $\langle \cos \gamma \rangle$. Our estimated rate of motion would then be

$$\frac{dr_f}{dt} = \langle \cos \gamma \rangle \frac{G(< r_f)}{dL_{\perp}(r_f)/dr}, \quad (12)$$

where r_f is the radius of the alignment front and $G(< r)$ is the magnitude of the torque integrated over the matter interior to r . At the order of magnitude level, $dr_f/dt \sim \Delta r_f \omega$, where Δr_f , the radial width of the alignment front, is $\sim r_f$ in BP-m. This estimate might also be further reduced by an allowance for some of the torque being deposited at radii between where it is given to the disk and the alignment front. However, if the transition region from an aligned inner disk to the inclined outer disk is reasonably narrow, this loss may not be very large. Confirmation of this guess is provided in Figure 14, where we show the track of an alignment front moving at the speed we estimate assuming $\langle \cos \gamma \rangle = 0.5$. As can be seen, it follows the contour of half-alignment quite well.

This model as stated implicitly assumes that the angular momentum given the disk by the external torques is instantaneously mixed radially across the entire transition region. In reality, of course, the mixing speed is of order the radial flow speed, which, we have argued, is roughly the sound speed in the presence of nonlinear warps. However, as shown by Sorathia et al. (2013), the Mach number of these radial motions is quite sensitive to $\hat{\psi}$ and the radial width of the warp, so that the sound speed is at best a rather crude estimator of the mixing speed. Nonetheless, in the conditions of BP-m, the sound speed is 3–6 \times larger than the alignment front speed, so that our instantaneous delivery approximation has little effect. A slower sound speed might lead to a narrower transition region.

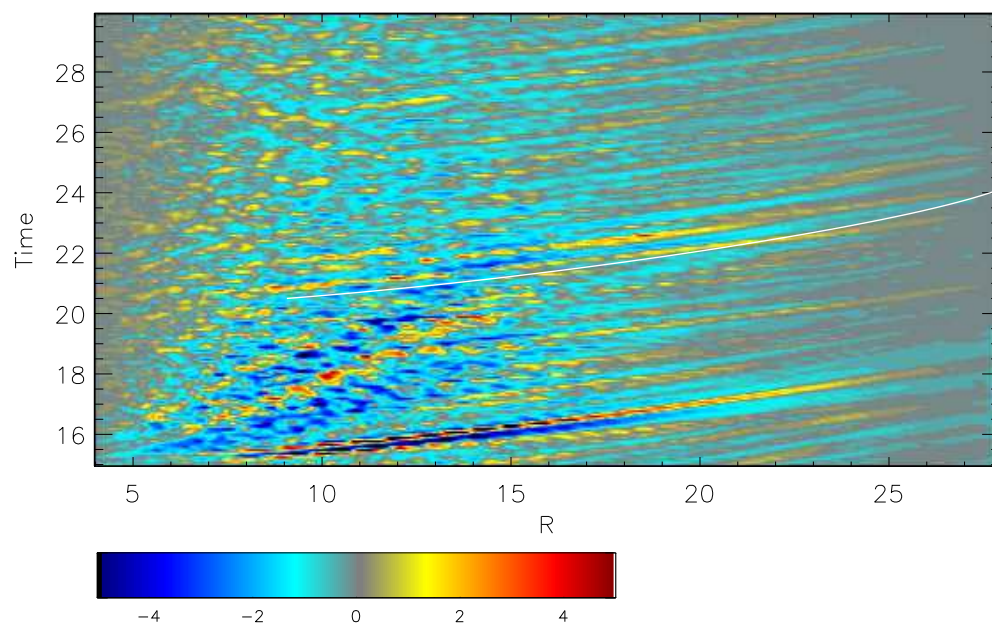


Fig. 13.— Color contours (see color bar) of $\partial \ln L_{\perp} / \partial t$ in BP-m. The white curve shows the trajectory of a sound wave traveling radially outward.

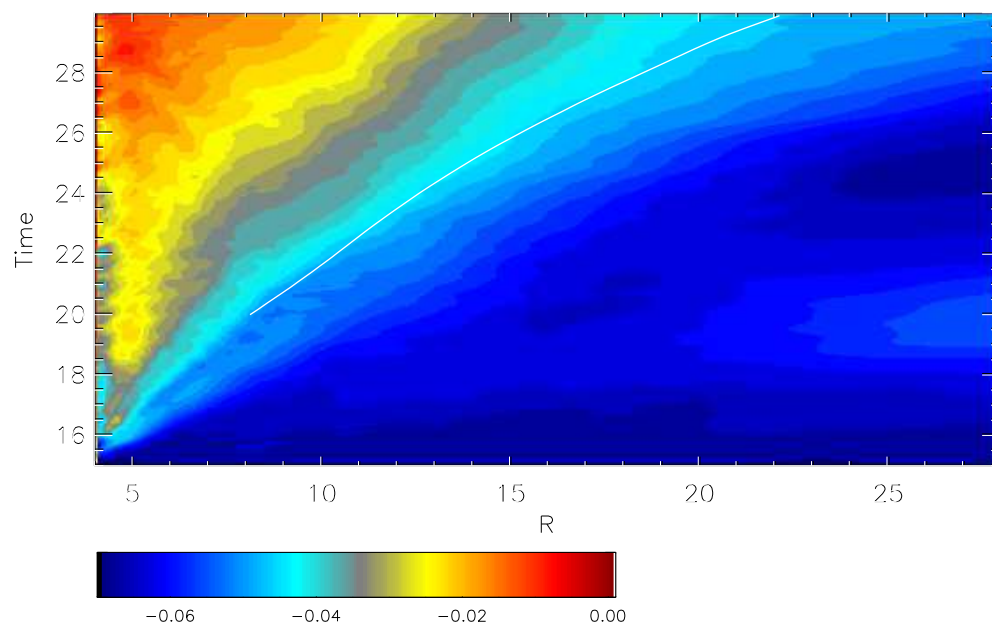


Fig. 14.— Color contours (see color bar) of the inclination angle (in units of π) in BP-m. The white curve shows the path of the alignment front traveling at the speed indicated by Eqn. 12.

4.2. Alignment, stalled and completed

As is readily apparent in Figure 5, although BP-h diminishes its misalignment, it is never able to remove more than $\simeq 40\%$ of its tilt, whereas BP-m continuously eliminates the offset between its angular momentum direction and the central mass’s spin, achieving hardly any difference between the two throughout its inner radii by the end of the run. Given that even in BP-m magnetic forces are thoroughly dominated by pressure forces, what accounts for this contrast?

We suggest that the answer lies in a combination of two facts. First, as we have already mentioned, the HD case rapidly achieves a state in which it precesses nearly as a solid-body. In the MHD case, by contrast, turbulence interferes with the ability to enforce solid-body rotation. As a consequence, in BP-h but not BP-m the direction of the planar angular momentum brought to a given radius is close to the direction of precession torque. In the language of the preceding section, after the first ~ 5 orbits or so, $\cos \gamma \simeq 0$ in BP-h.

Second, as found by Sorathia et al. (2012), the Reynolds stresses capable of mixing angular momentum radially are strongly increasing functions of disk warp when $\hat{\psi} > 1$. Below that level of warp, the radial pressure gradients are incapable of driving radial motions to speeds comparable to or greater than the sound speed; above that level, such speeds are generically attained. Comparing Figures 5 and 4, one can see that alignment drastically slows in the HD case when $\hat{\psi}$ drops below unity, in line with the expectation that when the tilt angle becomes $< H/r$, the warp-induced Reynolds stresses weaken. Because a purely hydrodynamic disk is always laminar, the alignment process therefore stops at this point. The MHD case differs because the magneto-rotational instability insures ubiquitous turbulence. Even where $\hat{\psi}$ is too small to drive strong radial flows, MHD turbulence nonetheless continues to mix neighboring regions. It is this process that allows MHD turbulence to complete the work of alignment after Reynolds stresses reduce the misalignment angle to be only of order the disk aspect ratio.

4.3. The inclination transition radius in an accreting disk

We have already estimated the alignment speed in terms of the torque integrated interior to some radius relative to the unaligned angular momentum at that radius. Presumably, if we had run simulation BP-m still longer, the alignment front would have propagated all the way out through our finite disk, and that would have been the end of further evolution. In real disks, however, the reservoir of matter with inclined angular momentum extends much farther out, and new unaligned matter is continually fed from the outside, while matter

already in the disk gradually moves inward toward the central object. Because the alignment speed inevitably must diminish outward as the torques weaken, in such a disk an outwardly moving alignment front would eventually find itself moving so slowly relative to the inward flow of misaligned angular momentum that its motion relative to the central mass would be reduced to zero. Thus, in a disk with time-steady accretion, both in terms of mass inflow and orientation, and a central object with a mass very large compared to the accreted mass, the disk would bend from its initial orientation to the orientation of the central object’s angular momentum at a fixed transition radius where these two speeds cancel.

The local torque scales with the surface density and $\sin \beta$, for misalignment angle β . The local misaligned angular momentum does likewise. Because the alignment front propagation speed is proportional to the ratio between the integrated torque interior to a given radius and the misaligned local angular momentum, it is therefore

$$\frac{dr_f}{dt} = \frac{2\langle \cos \gamma \rangle a_* (GM)^2}{\sin \beta(r) c^3 r^{3/2} \Sigma(r)} \int_0^r dr' \sin \beta(r') \Sigma(r') / r'^{3/2} \quad (13)$$

for black hole spin parameter $a_* \equiv a/M$.

In real disks, fresh misaligned angular momentum can be brought inward either by accretion of new material or by warp-induced radial flows; gravitational interaction with a binary companion or the mass of the outer disk may also contribute (Tremaine & Davis 2013). Outward motion of the alignment in mass terms can then be brought to a halt in terms of position when that inward speed matches the outward progress of the alignment front. Parameterizing the characteristic timescale of the inward advection of misaligned angular momentum by t_{in} , we find that the time-steady position of the inclination transition can be estimated as

$$R_T/r_g = \left[2\langle \cos \gamma \rangle a_* \Omega(R_T) t_{\text{in}} \int_0^1 dx x^{-3/2} \frac{\sin \beta(x) \Sigma(x)}{\sin \beta(R_T) \Sigma(R_T)} \right]^{2/3}, \quad (14)$$

where $r_g \equiv GM/c^2$ and the integral has been nondimensionalized by setting $x = r'/r = r'/R_T$.

The dimensionless integral may often have a value rather greater than unity. Partly this is due to an effect we have already pointed out, that the rapid increase inward of the precession frequency allows inner radii that are already nearly aligned to account for a significant part of the total torque. In addition, however, in some commonly-encountered accretion regimes, the surface density also increases inward (in time-steady accretion, for example, $\Sigma \propto x^{-3/5}$ when gas pressure dominates radiation pressure and the principal opacity is electron scattering). The dimensionless integral would then be rather greater than unity when the outermost part of the transition region lies at a radius a factor of a few or more

greater than the innermost part. This happens, for example, in the later stages of BP-m when r_f (as defined by the white curve in Fig. 14) passes the radius of maximum surface density, $r \simeq 10$. From then onward, the dimensionless integral is > 1 , reaching $\simeq 5$ or more by the end of the simulation, when $r_f \simeq 22$. However, we caution that this is at best illustrative: the detailed shape of the alignment transition is likely to be influenced by a number of factors: in addition to the shape of the radial surface density profile, the disk thickness profile, and perhaps other variables may also matter.

If the dominant misaligned angular momentum inflow mechanism is accretion, the inflow speed $v_{\text{in}} \simeq \alpha(h/r)^2 v_{\text{orb}}$, where α is the usual ratio between integrated internal (Maxwell) stress and integrated pressure, h/r is the local aspect ratio of the disk, and v_{orb} is the Keplerian orbital velocity. In this case, we find

$$R_T/r_g = \left[\frac{2\langle \cos \gamma \rangle a_*}{\alpha(h/R_T)^2} \int_0^1 dx x^{-3/2} \frac{\sin \beta(x)}{\sin \beta(R_T)} \frac{\Sigma(x)}{\Sigma(R_T)} \right]^{2/3}. \quad (15)$$

At the order of magnitude level, this estimate is consistent with the original estimate given by Bardeen & Petterson (1975) and Hatchett et al. (1981), although there are also ways in which our estimate differs from theirs. In particular, we note the quantitative importance of the dimensionless integral in equation 15.

Not long after these original estimates, Papaloizou & Pringle (1983) argued that the radial flows driven by warping should carry misaligned angular momentum much more rapidly than the mass flow of accretion. Moreover, in the model presented by that paper and elaborated by many since (Pringle 1992; Nelson & Papaloizou 2000; Lodato & Pringle 2007), the inward mixing can be described as a diffusion process with effective diffusion coefficient $\alpha_2 \simeq 1/(2\alpha)$ when $\alpha \ll h/r$. In that case, the estimate for R_T/r_g is (modulo the dimensionless integral) identical to that of eqn. 15, but multiplied by $\alpha^{4/3}$.

However, our previous study of purely hydrodynamic warp relaxation (Sorathia et al. 2013) demonstrated that, while the radial mixing of misaligned angular momentum qualitatively resembles diffusion, it differs from diffusion in a number of quantitative aspects; even in SPH simulations with an isotropic viscosity, the diffusion approximation appears to break down for nonlinear warps (Lodato & Price 2010). In addition, as shown in Section 3.4 of this paper, there are no stresses limiting the radial motions in a fashion described by an isotropic “ α -viscosity”; consequently, there is no reason to expect the radial mixing to scale $\propto \alpha^{-1}$.

A better estimate of the inward mixing rate might be $\sim c_s^2/v_{\text{orb}}(r_f/\Delta r_f)^2$, similar to the speed Nelson & Papaloizou (2000) identify with the case in which $\alpha \sim h/r$. This estimate is also closer to the rate found by Lodato & Pringle (2007) and Lodato & Price (2010) when α was small; in that limit, their SPH simulations with an isotropic α viscosity indicated that

α_2 saturated at $\simeq 3$. The basis of our estimate is that, as found in Sec. 4.1, $\hat{S}_{r\perp} \sim h/\Delta r_f$ because nonlinear warps generically create transonic radial flows, and they can travel a distance $\sim h$ in radius before being turned back by gravity. It must be recognized, however, that this is a very rough estimator, as it hides the fact that the magnitude of the misaligned angular momentum flux also depends on the shape of the transition region (Sorathia et al. 2013). The simulation data presented here do not bear directly on the effectiveness of inward mixing because the adherence of the alignment front propagation to our model (as well as the detailed radial dependence of the angular momentum flux) demonstrates that inward radial mixing plays at most a minor role in BP-m. Thus, the best we can do here is place bounds on R_T : the estimate of equation 15 is likely a solid upper bound, while a rough lower bound is given by the same expression with $\alpha \sim 1$.

5. Conclusions

We have carried out the first calculation of the Bardeen-Petterson effect in which the internal stresses are grounded entirely in known physical mechanisms (i.e., Reynolds and Maxwell stresses), and the disk configuration is thin enough that warp relaxation can be separated from accretion. It is also the first calculation making use of physical internal stresses in which disk alignment is observed. As predicted early on by analytic arguments (Papaloizou & Pringle 1983), the heart of the mechanism is the creation of radial pressure gradients due to the warps induced by the radial gradient in the Lense-Thirring precession rate. These radial pressure gradients drive radial fluid flows that convey misaligned angular momentum with them. By radially mixing misaligned angular momentum, these flows help to bind together the disk, compelling it to rotate almost as a solid body. In addition, as these flows move outward through the disk, the direction of the misaligned angular momentum they carry can, given some departure from solid-body precession, become sufficiently opposed to the local direction that, when mixed, the result is a reduction in the net magnitude of misaligned angular momentum. In this fashion, the disk gradually aligns with the spin axis of the central mass, first in its inner portions and later at larger radii.

By contrasting a pair of matched simulations, one including MHD, the other including only pure hydrodynamics, we were able to highlight the effects due to MHD and clarify those depending only on hydrodynamics. When the local warp is nonlinear (the generic situation), the radial flows are always transonic in speed. Internal stresses other than pressure are much too small to significantly influence them; in particular, we find no evidence for anything resembling an “isotropic α viscosity” acting to limit these radial motions. Although the magnetic forces are always small compared to pressure forces, they nonetheless have a

significant effect on both disk precession and the rate at which disks align with the angular momentum of the central mass they orbit. In particular, MHD effects cause more rapid alignment and more complete alignment—hydrodynamic alignment appears to stall when the offset angle falls to a value comparable to the disk aspect ratio H/r .

We believe there are two reasons for this contrast, both due to the omnipresent MHD turbulence. The first is that MHD turbulence disrupts the phase coherence of bending waves without necessarily damping them. By doing so, it prevents the enforcement of solid-body precession that occurs in the purely hydrodynamic case. As a result, the angular momentum delivered at small radii has a component directed *antiparallel* to the misaligned angular momentum at the rather larger radii where that angular momentum is ultimately deposited by the radial flows. This is the central mechanism of alignment. Outward carriage of “corrective” angular momentum is essential because the Lense-Thirring torques diminish so rapidly with increasing radius that an inner radius with only a small remaining inclination may nonetheless feel a greater torque than a radius only a factor of a few farther away that has a considerably larger inclination. The second effect of MHD turbulence is that it continues to mix unaligned angular momentum, even when the local warp is small enough (less than a scale height) that the radial motions induced by pressure gradients due to the warp are weak.

Our detailed treatment of the disk’s internal dynamics also reveals that the flow of misaligned angular momentum within the disk is by no means smooth and regular. Radial fluxes of angular momentum are sharply increased when the radial gradients in the Lense-Thirring torque build a local disk warp whose angular contrast across a radius is at least as large as the disk scale height. The evolution of orientation at a fixed radius is therefore a sort of “stick and slip” process in which differential torque gradually builds local warp, which is then erased quickly when it becomes nonlinear. Radial propagation of angular momentum is further modulated by acoustic waves.

This picture suggests a model for the speed at which alignment in an initially-inclined disk moves outward: the speed of the alignment front $v_f \simeq 0.5G(< r)/(dL_{\perp}/dr)$, where the factor 0.5 comes from computing the mean (anti-)alignment between the angular momentum brought outward from the torqued regions and deposited at the alignment front. In a time-steady disk, the outward motion is eventually brought to a halt by inflow of misaligned angular momentum due to a combination of radial mixing induced by disk warp and the accretion flow itself. To order of magnitude accuracy, we can use this picture to estimate where the transition from inclined to aligned orbits takes place in a time-steady disk. If all the uncertainties associated with the rate of inward misaligned angular momentum flux and the radial distribution of torque are wrapped into a single parameter Φ , we suggest

that its magnitude may be roughly bounded by $1 < \Phi < \alpha^{-2/3}$, where α is the usual time-averaged ratio of vertically-integrated r - ϕ stress to vertically-integrated pressure. The transition radius would then be found at $R_T \sim \Phi a_*^{2/3} (h/R_T)^{-4/3} r_g$.

Acknowledgements

We would like to thank Cole Miller and Steve Lubow for extensive and valuable discussions. This work was partially supported under National Science Foundation grants AST-1028111 and AST-0908326 (JHK and KAS), AST-0908869 (JFH), and NASA grant NNX09AD14G (JFH). The National Science Foundation also supported this research in part through XSEDE resources on the Kraken cluster through Teragrid allocation TG-MCA95C003.

REFERENCES

- Balbus, S. A., & Hawley, J. F. 1991, *Astrophysical Journal*, 376, 214
- . 1998, *Reviews of Modern Physics*, 70, 1
- Bardeen, J. M., & Petterson, J. A. 1975, *ApJ*, 195, L65
- Brandenburg, A., Nordlund, A., Stein, R. F., & Torkelsson, U. 1995, *ApJ*, 446, 741
- Fragile, P. C., & Anninos, P. 2005, *ApJ*, 623, 347
- Fragile, P. C., & Blaes, O. M. 2008, *ApJ*, 687, 757
- Fragile, P. C., Blaes, O. M., Anninos, P., & Salmonson, J. D. 2007, *ApJ*, 668, 417
- Hatchett, S. P., Begelman, M. C., & Sarazin, C. L. 1981, *ApJ*, 247, 677
- Hawley, J. F. 2000, *ApJ*, 528, 462
- Hawley, J. F., Gammie, C. F., & Balbus, S. A. 1995, *Astrophysical Journal* v.440, 440, 742
- Hawley, J. F., Guan, X., & Krolik, J. H. 2011, *ApJ*, 738, 84
- Hawley, J. F., & Stone, J. M. 1995, *Computer Physics Communications*, 89, 127
- Lodato, G., & Price, D. J. 2010, *MNRAS*, 405, 1212

- Lodato, G., & Pringle, J. E. 2007, MNRAS, 381, 1287
- Lubow, S. H., Ogilvie, G. I., & Pringle, J. E. 2002, MNRAS, 337, 706
- Nelson, R. P., & Papaloizou, J. C. B. 2000, MNRAS, 315, 570
- Nixon, C., King, A., Price, D., & Frank, J. 2012, ApJ, 757, L24
- Noble, S. C., Krolik, J. H., & Hawley, J. F. 2010, The Astrophysical Journal, 711, 959
- Ogilvie, G. I. 1999, MNRAS, 304, 557
- Papaloizou, J. C. B., & Pringle, J. E. 1983, MNRAS, 202, 1181
- Pessah, M. E., Chan, C.-K., & Psaltis, D. 2008, MNRAS, 383, 683
- Pringle, J. E. 1992, MNRAS, 258, 811
- Sorathia, K. A., Krolik, J. H., & Hawley, J. F. 2013, ApJ, 768, 133
- Sorathia, K. A., Reynolds, C. S., Stone, J. M., & Beckwith, K. 2012, ApJ, 749, 189
- Stone, J. M., Hawley, J. F., Gammie, C. F., & Balbus, S. A. 1996, Astrophysical Journal v.463, 463, 656
- Stone, J. M., & Norman, M. L. 1992a, The Astrophysical Journal Supplement Series, 80, 753
- . 1992b, Astrophysical Journal Supplement v.80, 80, 791
- Torkelsson, U., Ogilvie, G. I., Brandenburg, A., Pringle, J. E., Nordlund, Å., & Stein, R. F. 2000, MNRAS, 318, 47
- Tremaine, S., & Davis, S. W. 2013, ArXiv e-prints

6. Appendix

In Figure 15, we show the density-weighted MHD resolution quality factors as functions of radius in BP-m at two times, one during the saturated MHD turbulence immediately prior to the beginning of the torques ($t = 14.5$) and one well into the evolution with torques ($t = 17$). The quality factors are defined as

$$Q_x = \frac{2\pi v_{A,x}}{\Delta x}, \quad (16)$$

where $v_{A,x}$ is the Alfvén speed restricted to the x -component of the magnetic field. Although the disk tilts out of the equatorial plane of the coordinate system as BP-m evolves past $t = 15$, at $t = 17$, only the smallest radii, $r \lesssim 6$ have changed their orientation in a noticeable way, so we make the approximation that the directions of the axes for the disk remain the coordinate axes.

At $t = 14.5$, $\langle Q_z \rangle_\rho \simeq 12$ –25, while $\langle Q_\phi \rangle_\rho \simeq 30$ –50. Although the magnetic field is significantly weakened immediately after the torques begin, at $t = 17$ the quality factors are still fairly good: $\langle Q_z \rangle_\rho \simeq 8$ –20, while $\langle Q_\phi \rangle_\rho \simeq 20$ –50. We also checked later times and found that they were not much different from $t = 17$ in terms of these numbers. Hawley et al. (2011); Sorathia et al. (2012) recommended that both Q_z and Q_ϕ should be $\gtrsim 10$ and preferably $\gtrsim 20$, but also remarked that a particularly large value of one could compensate for a smaller value of the other. On this basis, we regard the simulation as reasonably well-resolved throughout. However, it is possible, particularly when larger inclination angles are explored, that the quality factors required for resolving MRI-driven MHD turbulence may be different in warped disks.

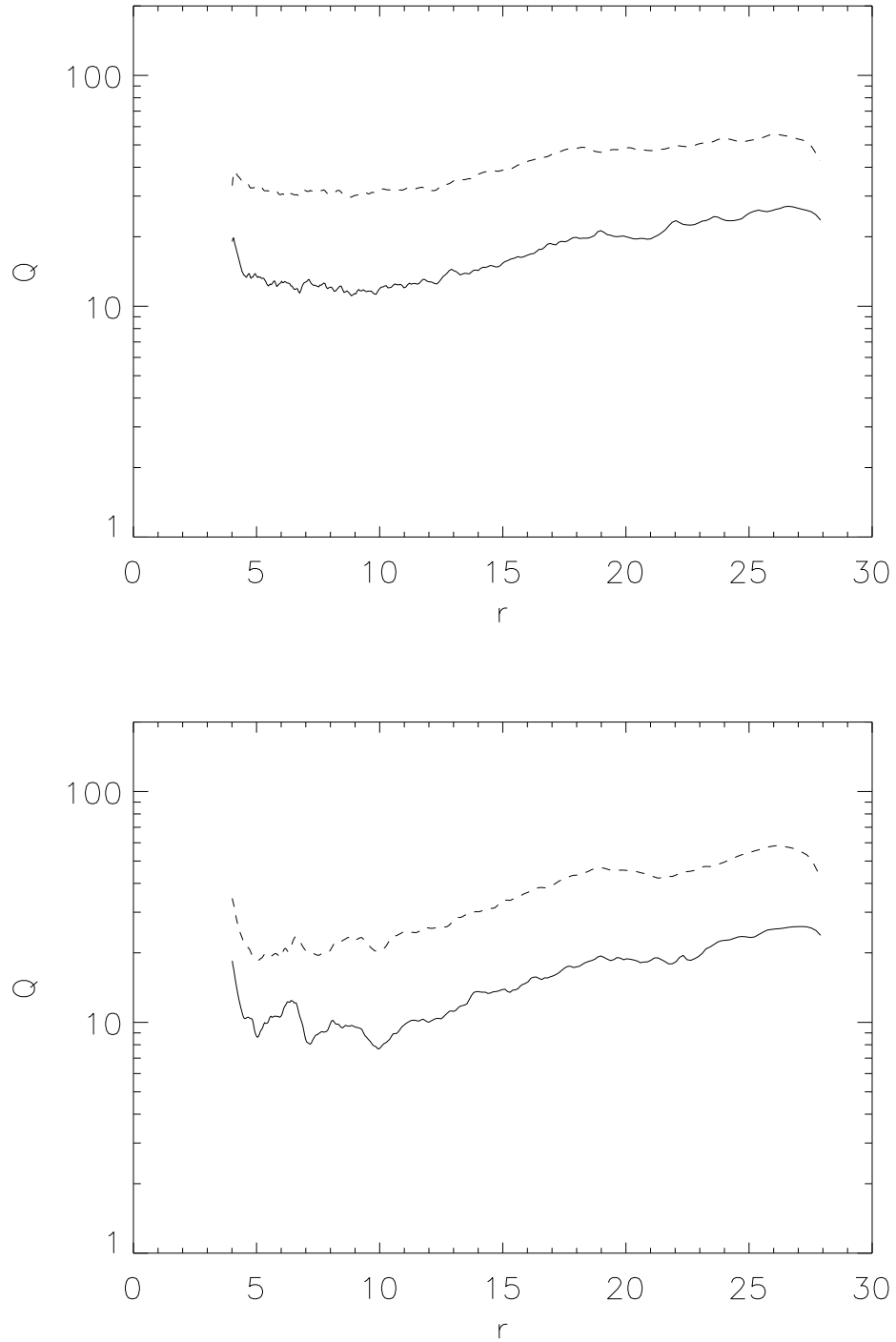


Fig. 15.— Density-weighted Q_z (solid curve) and Q_ϕ (dashed curve) at times $t = 14.5$ (upper panel) and $t = 17$ (lower panel) in BP-m. We define Q_ϕ as the quality factor in the azimuthal direction in the coordinate equatorial plane.